

A Finite-Difference GCM Dynamical Core with a Variable-Resolution Stretched Grid

MICHAEL S. FOX-RABINOVITZ AND GEORGIY L. STENCHIKOV

University of Maryland at College Park, College Park, Maryland

MAX J. SUAREZ

Goddard Space Flight Center, Greenbelt, Maryland

LAWRENCE L. TAKACS

General Sciences Corporation, Laurel, Maryland

(Manuscript received 30 December 1996, in final form 2 April 1997)

A finite-difference atmospheric model dynamics or dynamical core using variable resolution, or stretched grids, is developed and used for regional–global medium-term and long-term integrations.

The goal of the study is to verify whether using a variable-resolution dynamical core allows us to represent adequately the regional scales over the area of interest (and its vicinity). In other words, it is shown that a significant downscaling is taking place over the area of interest, due to better-resolved regional fields and boundary forcings. It is true not only for short-term integrations, but also for medium-term and, most importantly, long-term integrations.

Numerical experiments are performed with a stretched grid version of the dynamical core of the Goddard Earth Observing System (GEOS) general circulation model (GCM). The dynamical core includes the discrete (finite-difference) model dynamics and a Newtonian-type rhs zonal forcing, which is symmetric for both hemispheres about the equator. A flexible, portable global stretched grid design allows one to allocate the area of interest with uniform fine-horizontal (latitude by longitude) resolution over any part of the globe, such as the U.S. territory used in these experiments. Outside the region, grid intervals increase, or stretch, with latitude and longitude. The grids with moderate to large total (global) stretching factors or ratios of maximum to minimum grid intervals on the sphere are considered. Dynamical core versions with the total stretching factors ranging from 4 to 32 are used.

The model numerical scheme, with all its desirable conservation and other properties, is kept unchanged when using stretched grids. Two model basic horizontal filtering techniques, the polar or high-latitude Fourier filter and the Shapiro filter, are applied to stretched grid fields. Two filtering approaches based on the projection of a stretched grid onto a uniform one are tested. One of them does not provide the necessary computational noise control globally. Another approach provides a workable monotonic global solution. The latter is used within the developed stretched grid version of the GEOS GCM dynamical core that can be run in both the middle-range and long-term modes. This filtering approach allows one to use even large stretching factors.

The successful experiments were performed with the dynamical core for several stretched grid versions with moderate to large total stretching factors ranging from 4 to 32. For these versions, the fine resolutions (in degrees) used over the area of interest are 2×2.5 , 1×1.25 , 0.5×0.625 , and 0.25×0.3125 . Outside the area of interest, grid intervals are stretching to 4×5 or 8×10 . The medium-range 10-day integrations with summer climate initial conditions show a pronounced similarity of synoptic patterns over the area of interest and its vicinity when using a stretched grid or a control global uniform fine-resolution grid.

For a long-term benchmark integration performed with the first aforementioned grid, the annual mean circulation characteristics obtained with the stretched grid dynamical core appeared to be profoundly similar to those of the control run with the global uniform fine-resolution grid over the area of interest, or the United States. The similarity is also evident over the best resolved within the used stretched grid northwestern quadrant, whereas it does not take place over the least-resolved southeastern quadrant. In the better-resolved Northern Hemisphere, the jet and Hadley cell are close to those of the control run, which does not take place for the Southern Hemisphere with coarser variable resolution. The stretched grid dynamical core integrations have shown no negative computational effects accumulating in time.

The major result of the study is that a stretched grid approach allows one to take advantage of enhanced resolution over the region of interest. It provides a better representation of regional fields for both medium-term and long-term integrations.

Corresponding author address: Dr. Michael Fox-Rabinovitz, University of Maryland, Suite 200, 7501 Forbes Blvd., Seabrook, MD 20706.
E-mail: foxrab@dao.gsfc.nasa.gov

The developed stretched grid model dynamics is supposed to be the first stage of the development of the full diabatic stretched grid GEOS GCM. It will be implemented, within a portable stretched grid approach, for various regional studies with a consistent representation of interactions between global and regional scales and phenomena.

1. Introduction

The advantage of using nonuniform grids with enhanced resolution over the area of interest has been discussed in the context of regional modeling for years (e.g., Charney 1966; Anthes 1970). The downscaling with the *nested-grid* approach was applied first to regional forecast models (e.g., Phillips 1979; the review by Koch and McQueen 1987) and later to regional climate simulations (e.g., Pielke et al. 1992). The different versions of the Penn State-NCAR mesoscale model (MM4 and MM5) are most widely used.

Exceptions are the French (Courtier and Geleyn 1988; Yessad and Benard 1996) and Canadian (Staniforth and Mitchell 1978; Staniforth et al. 1991; Côté et al. 1993) operational models with variable-resolution stretched grids and the models developed by Paegle (1989) and the Krishnamurti group (Hardiker 1997).

For limited-area and nested-grid models, the problem of formulating well-posed or mathematically correct lateral boundary conditions, is far from resolved in spite of the four-decade-long effort since the pioneering paper of Charney et al. (1950). This difficult problem has been eloquently discussed by Robert and Yakimiw (1986), Oliger and Sundstrom (1978), Yakimiw and Robert (1990), Browning et al. (1973), Williamson and Browning (1974), and Staniforth (1995). As practical compromise solutions, some versions of the Davies (1976) technique are most widely used.

Successful nested-grid model integrations are known to be performed for short-term forecasts. After that, the forecast fields, especially near the fine-resolution area boundary, become contaminated by noise due to the abrupt change of resolution at the boundary. Applying strong filters will inevitably result in deteriorating the solution quality. In other words, the longer-term integrations suffer from an inaccurate interaction at the boundaries of the area of interest. Therefore, a nested-grid approach does not allow one to perform continuous long-term integrations without updating initial and boundary conditions.

However, nested-grid models are the first ones to be used successfully in recent pioneering studies on regional climate (e.g., Pielke et al. 1992). The only way of using these models to produce regional climate diagnostics is to periodically update initial and/or lateral boundary conditions after a short period of integration, that is, 1–2 days. Either observational analyses or global (or larger area) model forecast fields can be used for this purpose. These periodic updates of initial and lateral boundary conditions are a dominating forcing that results in a predominantly one-way interaction between the coarse- and fine-resolution areas. Actually, the fine-resolution fields may provide

only a marginal to moderate impact on the coarse-resolution fields within a buffer zone around the area of interest. Formally, boundary conditions could be of a two-way-interaction type for which the aforementioned problems still occurs. Along with using fine resolution, the success of nested grid models is based mostly on introducing a fine-resolution boundary condition forcing. Also, it is possible, within this approach, to use nonhydrostatic approximations for regional models.

Notice that periodic updates of initial conditions makes the regional integration procedure quite similar, in a sense, to that of an intermittent data assimilation with longer periods between data insertion. Namely, regional simulations are not continuous but intermittent, with regional climate diagnostics produced in between outer boundary and initial data insertions. The results depend on the type of boundary conditions used and the type and quality of inserted data.

Recently, the adaptive grid approach, originally developed for astrophysics, aeronautical, and other computational fluid dynamics problems has been discussed and applied to simple atmospheric models (e.g., Dietachmayer and Droegemeier 1992; Berger and Oliger 1984; Skamarock 1989; Skamarock et al. 1989). The first attempt to introduce a specific spherical adaptive grid to an atmospheric model was undertaken by Kurihara (1965). Apparently, the adaptive grid schemes can be beneficial for short-term forecasting, paying special attention to meteorological phenomena (like fast-moving cyclones) requiring enhanced resolution. However, for regional climate simulations, along with using finer-resolution fields, the most important impact is obtained by using fine-resolution orographic and other physical forcings over the *entire* area of interest. Such an impact can be negatively affected by the gridpoint redistributions applied for adaptive grids to keep the computational cost under control.

Another kind of variable-resolution model to be discussed in this study is based on a stretched grid approach. With such an approach, grid intervals outside a uniform fine-resolution area of interest are stretched uniformly over the rest of the globe. As a result, a single global variable-resolution grid is obtained. As an option, the spherical grid can be rotated so that the area of interest is located, on our choice, over the new, rotated equator area. Such an approach was introduced by Staniforth for finite-element models (e.g., Staniforth and Mitchell 1978; Cote et al. 1993; Gravel and Staniforth 1992; and Staniforth 1995).

For a gridpoint model with variable resolution, the stretched grid approach with the same model used over the entire globe seems to be attractive because it is free of the previously mentioned ill-posed problem typical for

nested grids. The associated additional computational cost due to stretching versus nesting is not overwhelming. For example, with a practically acceptable local stretching rate of about 5%–10%, which is a grid interval change between the adjacent grid points, the significant part or even majority of global grid points are usually located inside the area of interest for a variety of resolution versions.

Schmidt (1977) developed another stretched grid version for spectral models (e.g., Courtier and Geleyn 1988). Within this approach, a conformal coordinate transformation is introduced. For the French operational model, one transformed hemisphere with the pole located at central France contains western Europe, while another transformed hemisphere comprises the rest of the globe. For this model, using large total stretching factors of 7–10 works only for short-term forecasting (J.-F. Geleyn 1995, personal communication). Small to moderate stretching factors of 2 to 4 are used for promising, successful climate simulation with the spectral model (Déqué and Piedelievre 1995).

Having established the attractive advantages of the global stretched grid approach, the legitimate question to ask is what its limitations are. They should be considered in the context of various applications to regional forecasting, data assimilation, and climate simulation, as compared to the corresponding control runs with time-consuming global models with uniform fine resolution. Outside the fine-resolution area of interest, all scales are approximated with larger truncation errors; however, the small-scale motions dissipate quickly and their impact on the regional scales is small. Similar to the situation with limited-area models, one can assume that it takes a limited time for the incoming flow approximated on a variable-resolution stretched grid to reach, affect, and influence the flow over the area of interest. The regional flow will depend on interactions with such an incoming large-scale background circulation. A downscaling due to better resolved regional scales and regional forcing as well as their interactions will continuously play an important role over the area of interest. Notice that for the uniformly stretched grid, the incoming flow is better resolved and more effectively represented by gradually changing resolution than by a nested grid with an abrupt resolution change. Therefore, for stretched grids, the flow coming into the area of interest is better resolved, especially its large-scale and medium-scale components.

The key hypothesis to verify in this study is whether a significant downscaling or an adequate representation of regional scales is taking place over the area of interest (and its vicinity) for both short-, medium-, and, most importantly, long-term integrations with a variable-resolution (stretched grid) dynamical core.

In this study, the stretched grid approach is developed and tested for a finite-difference model. Namely, it was implemented to the Goddard Earth Observing System (GEOS) general circulation model (GCM) dynamical core (Suarez and Takacs 1995). The GEOS GCM numerical scheme, with all its desirable conservation and other prop-

erties, is kept unchanged when using stretched grids. The approach developed by Held and Suarez (1994) for testing dynamical cores is used in the study. Experimenting with a model dynamical core provides an ultimate test of computational properties of a model numerical scheme and its dependence on resolution, or more specifically, on stretching factors. Long-term dynamical core integrations are performed with the Newtonian-type rhs forcing (Held and Suarez 1994) as a substitution for model physics. Using model dynamical core integrations allows one to investigate the specific impacts of discretized model dynamics and resolution on full model errors, independently of full model physics.

In the context of verifying the key hypothesis outlined above, when testing the stretched grid dynamical core, we are pursuing the following goals. We are comparing, in both a medium-range forecast mode and a long-term climate mode, the results of stretched grid runs against the corresponding basic control runs with fine uniform global grids, especially over the area of interest and its vicinity. We should verify whether there is any degradation of the synoptic-scale patterns, produced by the control runs, by the stretched grid runs. We are also making sure that in a long-term integration mode there is no development of cumulative undesirable effects of a numerical nature related to stretched grid approximation of model dynamics. A particular emphasis is placed on ultimately using the stretched grid approach for future regional climate modeling applications.

Section 2 is devoted to discussing the basic numerical problems for variable-resolution, or nonuniform, stretched grids. A brief description of the numerical scheme and filtering procedures is given in section 3. Application of the filtering techniques and the results of long-term numerical experiments with the stretched grid dynamical core are presented in section 4. Middle-range integrations with large stretching factor grids are discussed in section 5. Concluding remarks are given in section 6.

2. A brief discussion of basic numerical problems for finite-difference approximations with variable-resolution stretched grids

The rationale for using irregular (nonuniform or nonequidistant) grids for approximations of atmospheric model dynamics has been discussed in the introduction. However, there are basic computational problems arising from grid irregularity. It affects the accuracy of approximation, computational stability, computational dispersion, and other properties of finite-difference schemes. These problems have been discussed since the 1970s in computational fluid dynamics publications (e.g., Roache 1976; Vichnevetsky 1987; Olinger and Sundstrom 1978; Fletcher 1988) for advection equations. For atmospheric models, the additional numerical problems arising for adjustment or wave equations using stretched grids are equally

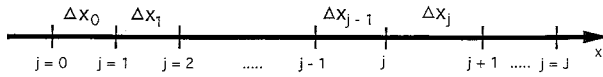


FIG. 1. The 1D nonuniform (nonequidistant) grid.

important (e.g., Anthes 1970, 1983; Staniforth 1995; Fox-Rabinovitz 1988).

In this section, we will make comments on the basic computational problems for finite-difference approximations related to grid irregularity for the 1D case.

a. Accuracy of approximation for spatial derivatives

To define a nonuniform, nonequidistant, stretched grid we need to introduce the local stretching rate or the ratio r_j of the adjacent grid intervals Δx_j and Δx_{j-1} (see Fig. 1):

$$r_j = \frac{\Delta x_j}{\Delta x_{j-1}}, \quad (1)$$

where $\Delta x_j = x_{j+1} - x_j$, $\Delta x_{j-1} = x_j - x_{j-1}$, and x is an independent variable. Note that $r_j \equiv 1$ for a uniform grid, and r_j is constant for all j 's for a *uniformly stretched* grid. For the latter, grid intervals change exponentially according to a geometric progression. Note also that $r_j > 1$ corresponds to a grid with stretching, or increasing grid intervals in the direction of increasing x (rightward), and $r_j < 1$ to stretching in the opposite direction. In the study, we use uniformly stretched grids with constant r_j 's. (Actually, a piecewise constant r_j 's will be used within a global stretched grid).

The local stretching rate r_j is the basic, defining local characteristic for a stretched grid. Another basic, fundamental parameter for a stretched grid is the *total* global stretching factor, or the ratio of the maximal to minimal grid intervals for the entire grid:

$$R = \frac{\Delta x_{\max}}{\Delta x_{\min}}. \quad (2)$$

This parameter represents the total amount of stretching for a grid.

Using irregular (nonuniform, nonequidistant) grids results in a loss of the accuracy of approximation (see, e.g., Roache 1976; Thompson 1984; Thompson et al. 1985; Fletcher 1988). For example, the well-known centered finite-difference approximation of the first derivative of a discrete function provides the second-order accuracy only for a uniform grid for which $\Delta x_j = \Delta x_{j-1}$ and $r_j = 1$.

For a nonuniform grid with $\Delta x_j \neq \Delta x_{j-1}$ and $r_j \neq 1$, the accuracy of approximation becomes only of the first order. For a nested grid, which is characterized by an abrupt change in resolution and, correspondingly, in the local stretching rate r_j , the second order

of approximation is lost completely. For a moderately smoothly stretched grid with r_j close to 1,

$$r_j = 1 + O(\Delta x). \quad (3)$$

Although the second order of approximation is formally lost, the accuracy of approximation is close to that of the second order. A similar loss in the accuracy of approximations takes place for higher derivatives of a discrete function and for higher orders of the accuracy of approximation.

b. Coordinate transformation from a physical to computational space

The coordinate transformation for the example of a uniformly stretched grid with $r_j = r = \text{constant}$ can be derived from geometric progression expressions for stretched grid intervals (see Fig. 1),

$$\Delta x_j = r^j \Delta x_0, \quad (4)$$

and for the coordinates of stretched grid points,

$$x_j = \Delta x_0 (1 + r + \dots + r^{j-1}) = \Delta x_0 \frac{r^j - 1}{r - 1}, \quad (5)$$

$$j = 1, 2, \dots,$$

where Δx_0 is the first grid interval starting from which the grid is stretching rightward, in the original physical space or coordinate system. In the transformed coordinate system, the original nonuniform grid becomes a uniform one, with the constant grid intervals for all j 's.

c. Comments on computational stability, dispersion, and wave propagation and reflection

For the same centered-difference schemes applied to both uniform and nonuniform grids, the CFL (Courant–Friedrichs–Lewy) computational stability criteria have similar forms. It is also true for computational dispersion characteristics. However, the substantial difference is that space intervals Δx are functions of x for nonuniform grids.

For the 1D linear advection equation approximated with a centered-difference scheme, the CFL computational stability criterion and the computational dispersion relation have the corresponding forms

$$\Delta t \leq \frac{\Delta x_{\min}}{c}$$

and

$$\nu = \frac{c}{\Delta x(x)} \sin[\kappa(x)\Delta x(x)], \quad (6)$$

where $c = \text{const}$ is the advection speed, ν the frequency, and κ is a wavenumber.

Therefore, a time step is controlled by the fine-resolution grid interval over the area of interest for

which $\Delta x_{\min} = \Delta x_o$ (Fig. 1). Note that using semi-implicit schemes is desirable for variable-resolution models to improve their computational efficiency.

Propagation and reflection of a wave group envelope, or wave packet, in a uniformly stretched grid (Fig. 1) for the linear 1D advection equation approximated with either a centered-difference or the Crank–Nicolson scheme, has been thoroughly investigated in a seminal paper by Vichnevetsky (1987).

It is worth noting that an interesting computational reflection effect for a wave packet takes place for the grid with the finest grid interval in the vicinity of $x = 0$ and with grid increments increasing monotonically and symmetrically in both directions from that point. For the initially rightgoing wave group, the reflection occurs at the point x_R with the group velocity $G = 0$. The resulting motion becomes leftgoing and the second reflection occurs at a symmetric point $-x_R$ where also $G = 0$. Therefore, the energy is trapped in the domain $(-x_R, x_R)$ in a kind of a “well.” This effect of the double reflection or “wave trapping” was first shown by Giles and Thompkin (1985).

Finally, for nonuniform grids, a spurious scattering effect takes place. It is enhanced for a nonuniformly stretched grid with $r_j \neq \text{const}$, as discussed by Vichnevetsky and Turner (1991).

A general solution for these computational problems arising from grid irregularity is to introduce diffusion-type filters and uniformly stretched grids. These are necessary tools for controlling the different kinds of computational noise discussed in this section (e.g., Vichnevetsky 1987; Fox-Rabinovitz 1988). Specifically, small-scale components of the flow and their transformations should be carefully controlled.

3. The GEOS GCM dynamical core with a stretched grid

The study is done using the GEOS GCM dynamics or dynamical core with a stretched grid. The model numerical scheme, with all its desirable conservation and other properties, is kept unchanged when using stretched grids. Using the dynamical core allows us to address the numerical problems due to grid irregularity on the sphere in the medium-range and long-term integration modes. The finite-difference dynamical core originally developed by Suarez and Takacs (1995) for a uniform grid, with a possibility to run it on nonuniform grids, is used in the study. The design of the filters to run on stretched grids is one of the main objectives of the study.

a. Brief description of the dynamical core

The model dynamical core has been developed by Suarez and Takacs (1995) as a module updating the time tendencies to include the adiabatic effects of the dynamics. The strict modular approach is intended to

allow for implementing the “plug-compatible” rules introduced in Kalnay et al. (1989) for structuring model physics parameterizations. The designed dynamical core is nearly “plug compatible.” It is used as a model dynamics component in the GEOS GCM (Takacs and Suarez 1996).

For our experiments, we adopted the approach developed by Held and Suarez (1994) for calculations with dynamical cores. Along with model dynamics, all model filters and a time stepping, or a state variable update, are implemented. Moreover, as a substitution for model physics, it also includes a simple linear damping of the velocities in lower model layers and temperature relaxation to a prescribed “radiative equilibrium” (Held and Suarez 1994). This Newtonian-type temperature forcing depends on latitude and pressure and is symmetric for both hemispheres about the equator.

More specifically, the previously mentioned damping and relaxation terms are introduced in the momentum and energy equations, respectively, in the form (Held and Suarez 1994)

$$\begin{aligned} \frac{\partial \mathbf{v}}{\partial t} &= \dots - \kappa_v(\sigma) \mathbf{v} \\ \frac{\partial T}{\partial t} &= \dots - \kappa_v(\varphi, \sigma) [T - T_{\text{eq}}(\varphi, p)], \end{aligned} \quad (7)$$

where φ is the latitude, p the pressure, \mathbf{v} the wind vector, T the temperature, and

$$T_{\text{eq}} = \max \left\{ 200 \text{ K}, \left[315 \text{ K} - (\Delta T)_y \sin^2 \varphi - (\Delta \theta)_z \log \left(\frac{p}{p_0} \right) \cos^2 \varphi \left(\frac{p}{p_0} \right)^\kappa \right] \right\},$$

$$\kappa_T = \kappa_a + (\kappa_a - \kappa_s) \cos^4 \varphi \max \left(0, \frac{\sigma - \sigma_b}{1 - \sigma_b} \right),$$

$$\kappa_v = \kappa_f \max[0, (\sigma - \sigma_b)/(1 - \sigma_b)],$$

$$\sigma_b = 0.7, \quad \kappa_f = 1 \text{ day}^{-1}, \quad \kappa_a = \frac{1}{40} \text{ day}^{-1},$$

and

$$\kappa_s = \frac{1}{4} \text{ day}^{-1}, \quad (\Delta T)_y = 60 \text{ K}, \quad (\Delta \theta)_z = 10 \text{ K},$$

$$p_0 = 1000 \text{ mb}, \quad \kappa = 2/7, \quad c_p = 1004 \text{ J kg}^{-1} \text{ K}^{-1}. \quad (8)$$

The temperature T_{eq} is symmetric about the equator. The friction and relaxation coefficients κ_v and κ_f decrease with height and in the boundary layer reach the maximum values of 1 day^{-1} and $\frac{1}{4} \text{ day}^{-1}$, respectively.

For a finite-difference approximation, the horizontal staggered Arakawa C grid (Mesinger and Arakawa 1976) and the vertical staggered Lorenz (1960) grids

are used. Basically, the numerical scheme is close to that of the UCLA GCM. The equations of motion are written in the form used by Sadourny (1975), Burridge and Haseler (1977), and Arakawa and Lamb (1981). Using some simplified assumptions, the scheme provides conservation of energy and potential enstrophy. The continuity thermodynamic and moisture equation approximations provide conservation of mass, potential temperature, and moisture (Suarez and Takacs 1995). For a uniform grid, the scheme is of a second-order, except for the horizontal advection of vorticity and potential temperature by the rotational component of the flow, which is of a fourth-order accuracy (Suarez and Takacs 1995; Takacs and Suarez 1996).

In the vertical, there are 20 sigma levels (Phillips 1957) spaced as in the GEOS GCM (Takacs et al. 1994). The vertical differencing is done according to the Arakawa and Suarez (1983) conservation scheme. The time-integration scheme employs the leapfrog scheme and a Robert–Asselin time filter (Robert 1966; Asselin 1972). It is combined with the economical explicit scheme (Brown and Campana 1978; Schuman 1971; Fox-Rabinovitz 1974). Following Brown and Campana (1978), a three-time-level averaging operator is applied to the pressure gradient force to provide stricter control of gravity wave instability. It results in using larger time steps and does not require any significant changes in the numerical scheme, except for introducing the certain order in which the model equations are integrated. The dynamical core structure allows for the pole rotation (Takacs and Suarez 1996) so that the area of interest can be located away from the poles and near the equator, for example. A stretched grid design and the corresponding polar and Shapiro filter modifications for a stretched grid are described below.

b. Stretched grid generation

Relying upon considerations discussed in section 2, the smooth, uniformly stretched grid has been designed for dynamical core experiments. In other words, the local stretching rate r_j [Eq. (1)] is kept constant and within not more than a 5%–10% deviation from unity. The total global stretching factor R [Eq. (2)], or the ratio of the coarsest to finest grid increments used in the experiments, ranges from moderate to large values of 4 to 32.

The area of interest contains a uniform fine-resolution latitude–longitude grid. It allows us to resolve maximally the regional prognostic fields as well as orographic and other physical boundary forcings. On the opposite side of the latitudinal circles covering the area of interest, we have only one coarse-resolution grid interval. In between the area boundaries and this maximally remote grid interval, the grid intervals are uniformly stretched (Fig. 2). Namely, the grid intervals $h(x)$ depend on x as $h(x) = h_{\min} + \alpha x$, where $\alpha = r - 1$ and h_{\min} is the minimal grid interval over the area of interest. This stretching on both left and right sides from the area of interest is done with constant

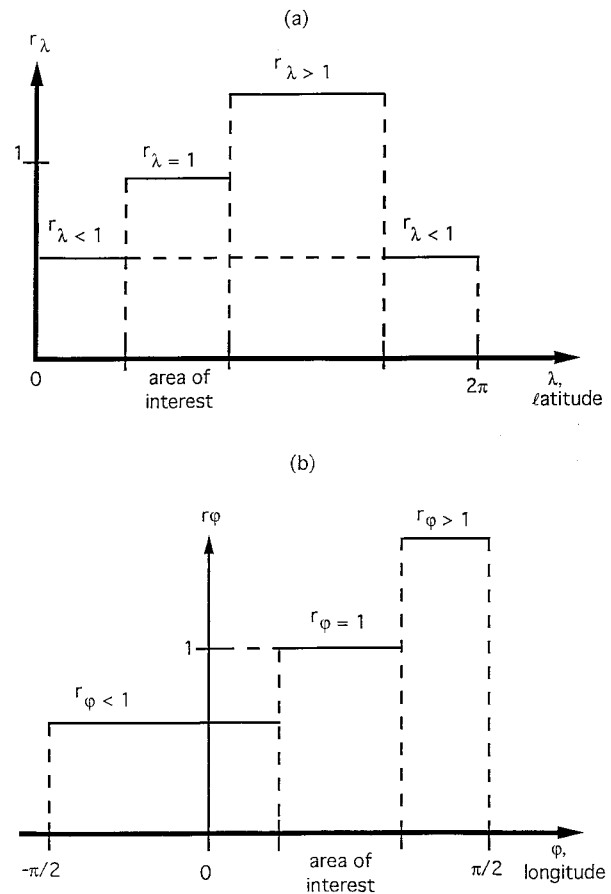


FIG. 2. The latitudinal (a) and longitudinal (b) stretching factors as piecewise constant functions.

local stretching rates r . More specifically, for the grid design, the grid intervals increase from the right boundary to the farthest, coarse grid interval with a constant local stretching rate r_λ . If one continues to move from the coarse grid interval to the left boundary, the grid intervals decrease with the constant local rate $r = 1/r_\lambda$. As a result, the local stretching rate for a latitudinal circle covering the area of interest is actually a piecewise-constant function (Fig. 2a). Namely, $r \equiv 1$ over the area of interest, $r = \text{const} > 1$ from the right boundary to the farthest, coarse grid interval, and $r = 1/\text{const} < 1$ from the farthest, coarse grid interval to the left boundary.

For the longitudinal circles covering the area of interest, the stretching procedure is quite similar. Starting from the area boundaries, the grid stretching is done with constant local stretching rates in both directions toward the poles. Therefore, for longitudinal circles covering the area of interest, the local stretching rate is also a piecewise-constant function (Fig. 2b). As a result, a stretched grid is defined globally, with arbitrary local stretching rates in both latitudinal and longitudinal directions. When the area of interest is shifted, or is nonsymmetric in respect to the equator, and the local stretching rates are the same in both directions, we obtain larger meridional grid intervals over

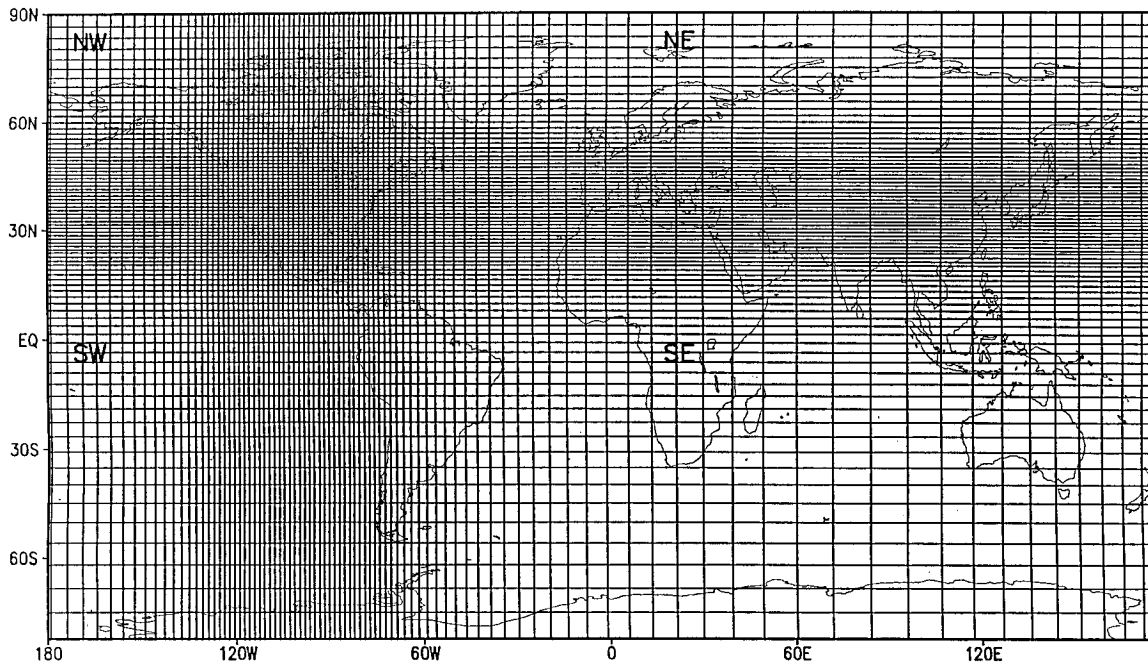


FIG. 3. The global stretched grid with the rectangular area of interest with fine resolution located over the United States region, or from 25° to 50°N and 125° to 75°W.

one of the poles than over the other. Therefore, when the area of interest is located near the pole, the coordinate rotation is desirable.

Practically, when generating a stretched grid, the total global stretching factor is introduced as the first input parameter, defined by setting the fine resolution over the area of interest and the coarse resolution over the farthest grid interval. Then, the input parameters for a rectangular (in latitude by longitude coordinates) area of interest are defined. The local stretching rates are calculated automatically by positioning the uniformly stretched grid points between the area of interest boundary and the remote coarse grid interval. The developed stretched grid generator automatically defines the grid with prescribed stretching parameters. Such a portable automated stretched grid generation procedure, with the previously mentioned input parameters, allows one not only to design stretched grids with different areas of interest and stretching parameters, but also to introduce time-dependent or moveable stretched grids an option similar to adaptive grids. The stretched grid used in this study is presented in Fig. 3. The area of interest is the rectangle covering the United States. For this stretched grid, the northwestern quadrant has the best variable resolution, whereas the southeastern quadrant is the least-resolved one. Two other quadrants have a medium variable resolution that is enhanced either in latitudinal or longitudinal direction.

For the grids considered in section 5, the computational gains are approximately 6, 10, and 16 times for the total stretching factors of 8, 16, and 32, correspondingly. The reduction of computation time for stretched grids versus the corresponding uniform fine-resolution grids depends

on the size of the area of interest (it could be only a part of the United States, for example). Also, the remote coarse-resolution area may contain not just one grid box, as considered above, but a significant part of the globe (e.g., Staniforth and Mitchell 1978; Cote et al. 1993). For different practically feasible stretched grids, the gains in computation time are ranging from several times to 1–2 orders of magnitude. In other words, using the stretched grid approach allows one to achieve such a variable fine regional–global resolution that is not possible otherwise (i.e., for uniform fine-resolution grids), even with the most powerful computers available now and in the foreseeable future.

c. The polar and Shapiro filters

Two horizontal filters are used at every time step (Takaacs et al. 1994). The first is a high-latitude, or polar, Fourier filter applied to all dependent variable tendencies. The polar filter allows us to avoid linear computational instability due to the convergence of the meridians near the poles. In other words, it prevents decreasing the time step due to a violation of a CFL criterion near the poles. The filter is applied poleward of 45° latitude. Its strength varies gradually when approaching the poles, by increasing the number and damping rate of affected zonal wavenumbers.

The Fourier transformation coefficients for a latitudinal circle are scaled by a filtering function

$$F = \left\{ \frac{\cos \varphi}{\cos(\pi/4) \sin[(i/l_M)(\pi/2)]} \right\}^2$$

$$i = 1, 2, \dots, l_M, \quad -\pi/2 \leq \varphi \leq \pi/2. \quad (9)$$

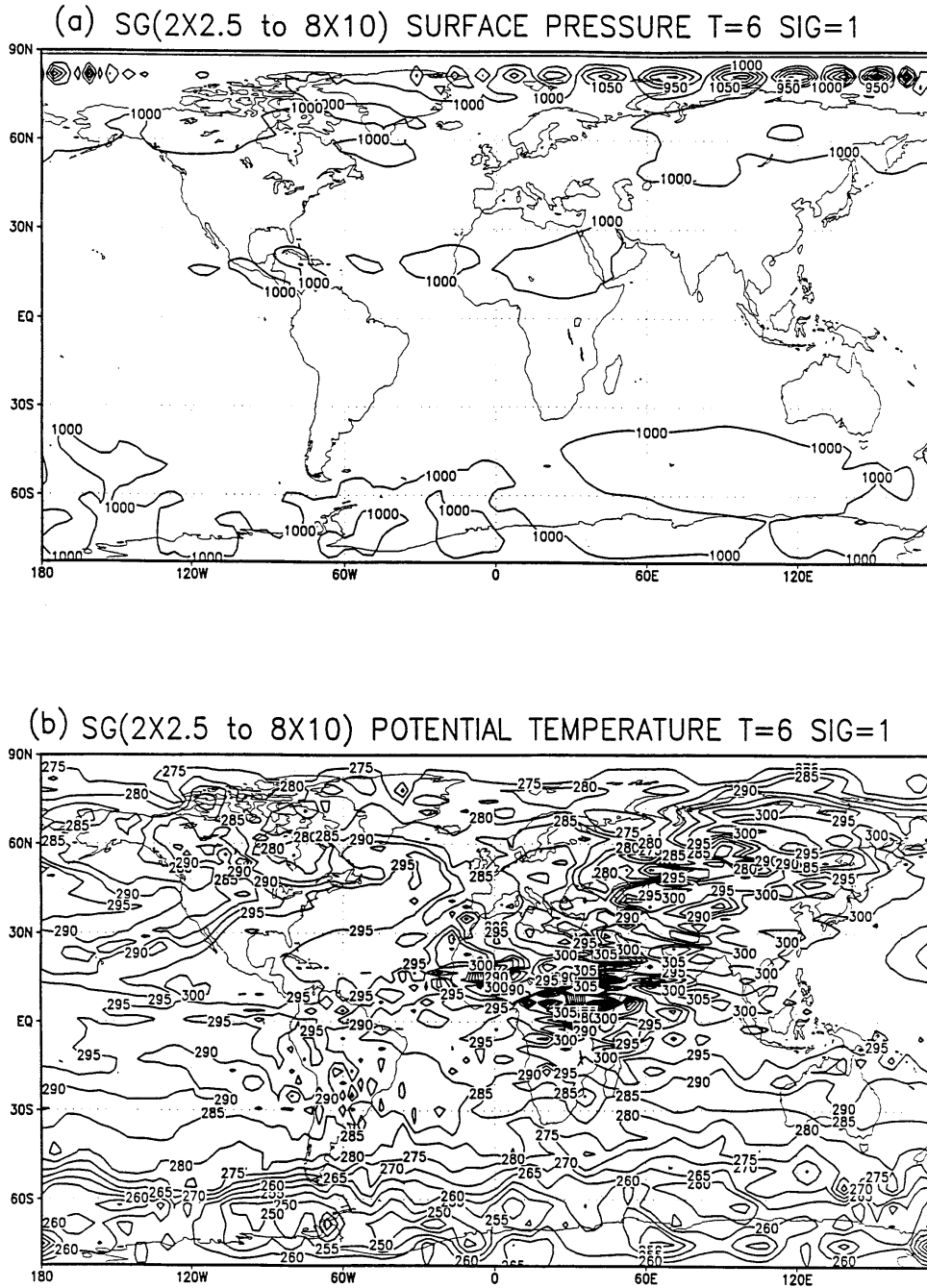


FIG. 4. The 6-day integration with the stretched grid dynamical core for the sea level pressure (a) and surface temperature (b), with filtering on the global uniform fine-resolution grid. The contour interval for the sea level pressure is 3 hPa and for surface temperature 3 K. Here, SG (2 × 2.5 to 8 × 10) stands for the stretched grid with uniform 2° × 2.5° resolution over the area of interest stretching to 8° × 10°. Note that in the absence of orography the sea level pressure and surface pressure are the same.

The filter strength can be increased by modifying the filtering function (12) in the following way:

$$F' = \left\{ \left[\frac{\cos \varphi}{\cos(\pi/4)} \right]^2 \frac{1}{\sin[(i/l_M)(\pi/2)]} \right\}^2 \quad (10)$$

It provides not only stronger but also spectrally wider filtering for the small-scale spectral range. It was used only for the experiments described in section 5 with the 0.5° × 0.625° and 0.25° × 0.3125° resolution over the area of interest but not for coarser-resolution runs.

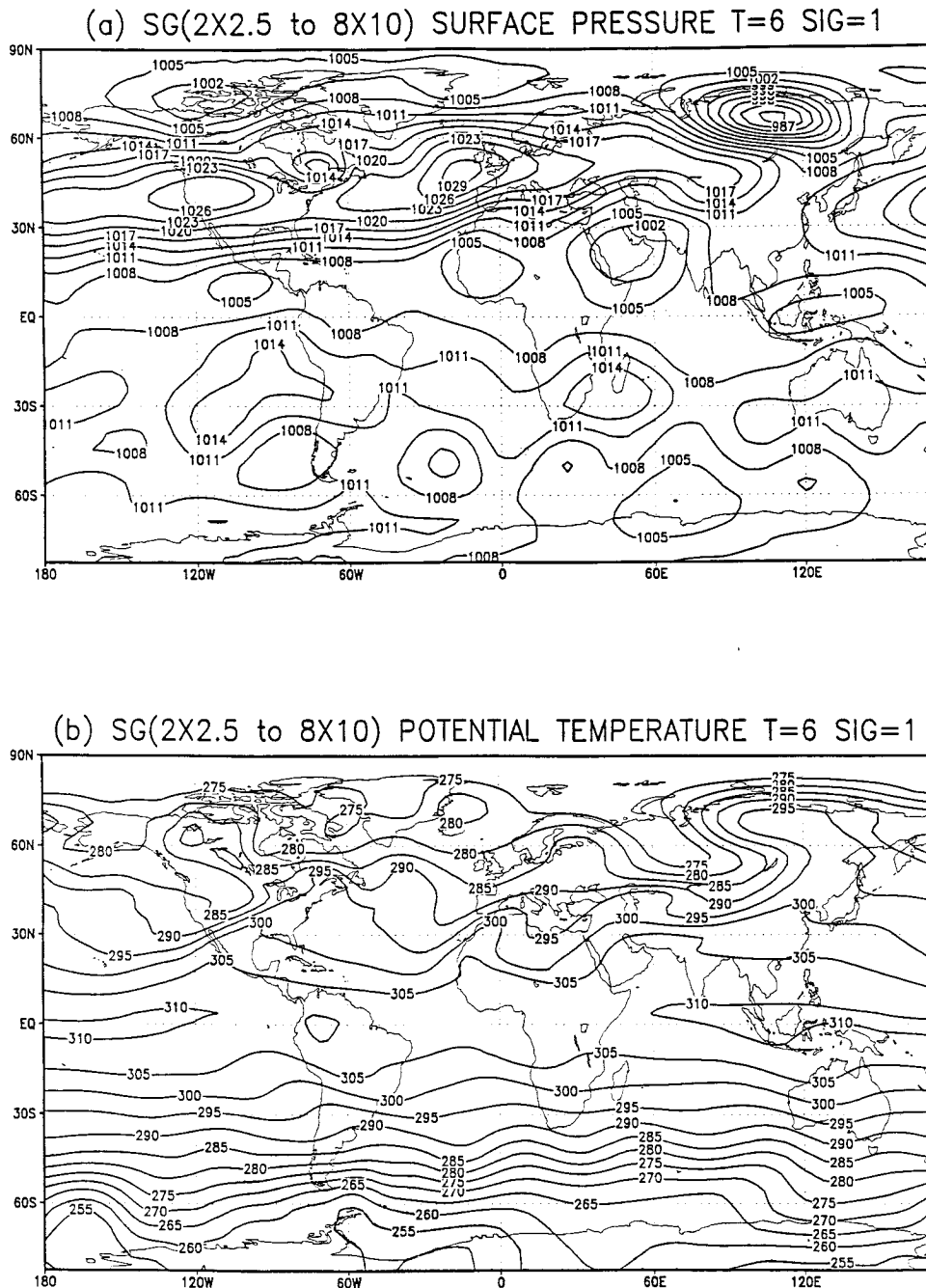


FIG. 5. The 6-day integration with the stretched grid dynamical core for the sea level pressure (a) and surface temperature (b), with direct filtering on the global stretched grid ($2^\circ \times 2.5^\circ$ stretching to $8^\circ \times 10^\circ$), using a coordinate transformation approach.

Another filtering technique used is the Shapiro (1970) filter. It is applied to all dependent variables, namely, to the winds, potential temperature, and surface pressure to damp globally small-scale dispersive waves. It also prevents the computational nonlinear instability (Phillips 1959) to occur. A Shapiro filter tendency $(\partial q/\partial t)_{SF}$ for a quantity q is

$$\left(\frac{\partial q}{\partial t}\right)_{SF} = \frac{q^F - q}{T}, \quad (11)$$

where q and q^F are unfiltered and filtered quantities, correspondingly, and the parameter T is an adjustable timescale. Thus, only a fraction $\Delta t/T$ of the full Shapiro filter is incorporated at each time step. Actually,

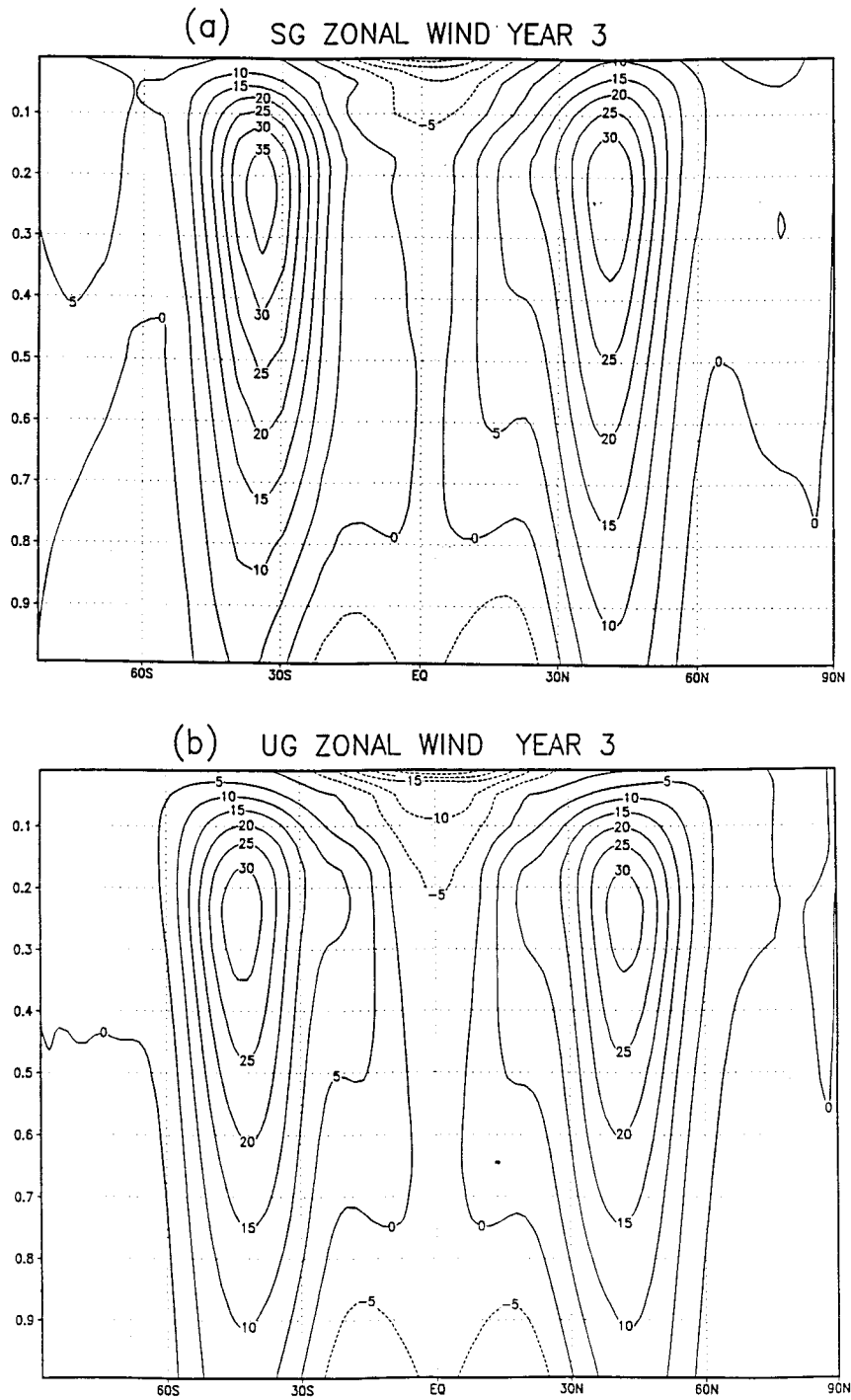
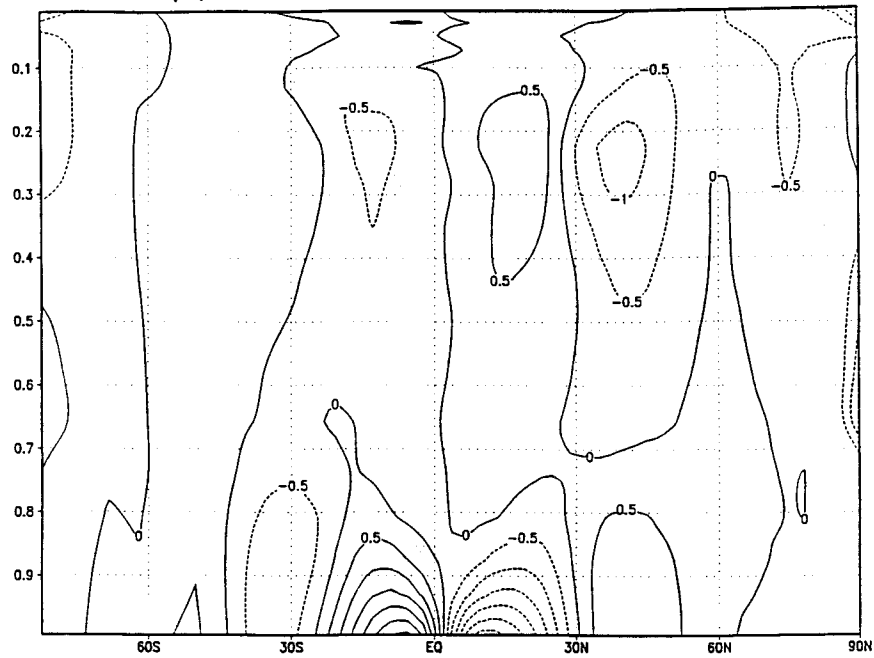


FIG. 6. The zonal annual mean (for the third year of the dynamical core integration, or year 3) vertical distribution of the zonal (a) and meridional (c) wind components for the stretched grid dynamical core run, with filtering on the stretched grid, using a coordinate transformation approach. (b) Same as in (a), and (d) same as (c) but for the control dynamical core run with the global uniform $2^\circ \times 2.5^\circ$ grid. The SG and UG stand for stretched grid and uniform fine-resolution grid, respectively. The negative values are shown by dashed lines. The contour interval for (a) and (b) is 5 m s^{-1} and for (c) and (d) 0.5 m s^{-1} .

(c) SG MERIDIONAL WIND YEAR 3



(d) UG MERIDIONAL WIND YEAR 3

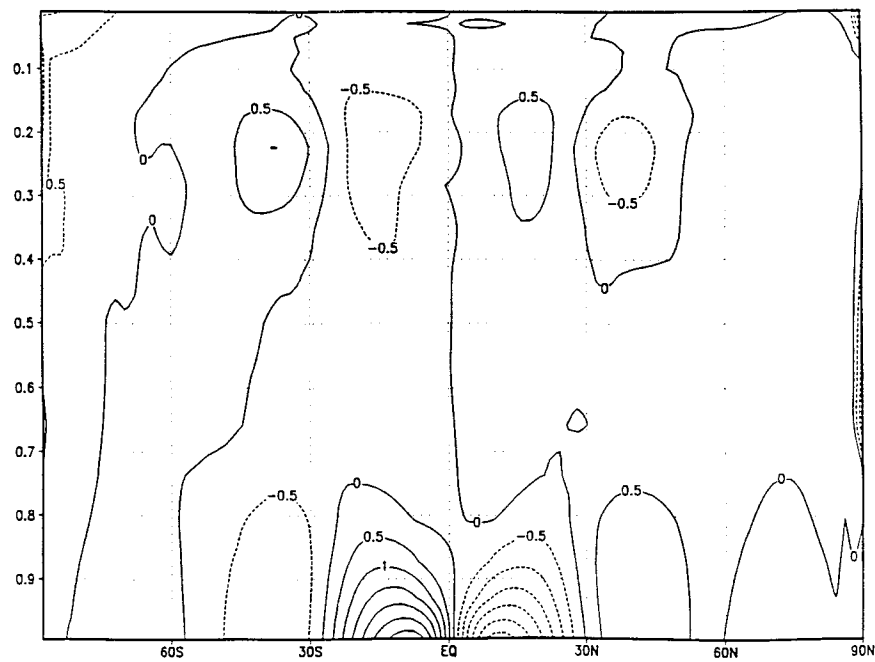


FIG. 6. (Continued)

$T = 1.5$ h is adjusted in such a way to remove the smallest two-grid-interval wave in approximately 6 h. The filter is applied separately in the longitudinal and latitudinal directions.

Its discrete form is

$$q_{i,j}^F = [1 - (F_\varphi^2)^n][1 - (F_\lambda^2)^n]q_{i,j}, \quad (12)$$

where

$$F_\lambda^2(q_{i,j}) = -\frac{1}{4}(q_{i+1,j} - 2q_{i,j} + q_{i-1,j}),$$

$$F_\varphi^2(q_{i,j}) = -\frac{1}{4}(q_{i,j+1} - 2q_{i,j} + q_{i,j-1}),$$

and n is a filter parameter. Note that $2n$ is a filter order. For $4^\circ \times 5^\circ$ and $2^\circ \times 2.5^\circ$ resolutions, the sixteenth- and eighth-order filters are applied, respectively (Takacs et al. 1994). Lower-order filtering corresponds to stronger damping. Usually, stronger noise is generated by a discretized model nonlinear dynamics when using finer resolution.

Since the Shapiro filter is not applied to surface pressure fields, the conservation of mass is not affected. The polar filter is applied only to the tendencies, but not forecast variables, and is conservative in the zonal direction (for which it is applied). The polar and Shapiro filters have only a small effect on total energy and potential enstrophy conservation. All that is true for the dynamical core with both uniform and variable resolution. These conservation properties were carefully checked for long-term integrations.

For the stretched grid versions of the dynamical core considered below, the strength of filtering, and, correspondingly, the filter order, is adjusted depending on horizontal resolution over the area of interest.

d. Filtering on a nonuniform grid

There are two practical ways to account for computational problems arising due to grid irregularity effects. In one approach, the coordinate transformation is applied to model governing equations and the corresponding numerical scheme. A grid transformation from nonuniform physical coordinates to orthogonal, uniform computational coordinates (see, e.g., Anthes 1970; Wilhelmson and Chen 1982) can be used. In another approach, the model governing equations and corresponding numerical scheme are not modified. This approach is used, for example, for the adaptive refinement method (e.g., Berger and Olinger 1984; Skamarock 1989; Skamarock et al. 1989).

In this study, the second approach with a smooth, uniformly stretched grid and no model numerical scheme modification is used. To account for actual grid irregularity and to control related computational noise, two simple versions of the existing model filtering techniques designed for uniform grids are tested. One of them, the interpolation approach, is based

on the global uniform fine-resolution filtering. Namely, the tendency fields obtained at every time step of the stretched grid model integration are interpolated first onto the global uniform fine-resolution grid. Next, standard polar and Shapiro filters are applied to the uniform grid. Then the resulting filtered fields are interpolated back onto the stretched grid.

Another version of the filtering procedure was interpreted above in terms of the coordinate transformation approach. When applied for filters only, it provides uniform filtering directly on a stretched grid. Namely, the polar and Shapiro filters are applied directly to the discrete or grid functions defined as global stretched grid fields, without interpolations to and from the global uniform fine grid. Actually, the specific coordinate transformation following from (5) for grid points is introduced by a stretched grid generator. In the transformed coordinate system, the stretched grid becomes uniform. All filtering is to be done for the grid.

Actually, it is not even necessary to make a formal transformation because the filters (9)–(12) do not depend on spatial coordinates (the same is true for the inverse transformation back to the physical space). The filters are applied to the grid functions or the stretched grid fields assuming that the grid is uniform in the transformed computational space. As a result, we control noise in a small-scale spectral range, which depends on variable resolution or stretched grid intervals $\Delta x(x)$.

4. Basic experiments with the stretched grid dynamical core

The goals of the experiments presented in this and the next section are as follows. We investigate the initial condition, or Cauchy problem, by running several-day integrations with realistic mean initial conditions and with two filtering techniques described above. We are running long-term benchmark integrations to analyze how they stabilize in time, compared to uniform grid runs such as those performed by Held and Suarez (1994). The long-term experiments are essential for the future regional climate applications. For medium-range integrations, the possibility of using large total global stretching factors without generating noise is tested. The integrations allow us to analyze the quality of the resulting fields versus the corresponding control experiments.

As a result of the aforementioned testing, the stretched grid dynamical core is prepared to introduce, at the future stages of the study, the orographic and other physical forcings within a stretched grid GCM.

All experiments with stretched grid model versions are performed with the grid shown in Fig. 3, with the rectangular area of interest located approximately over the United States, or from 25° to 50° N and 75°

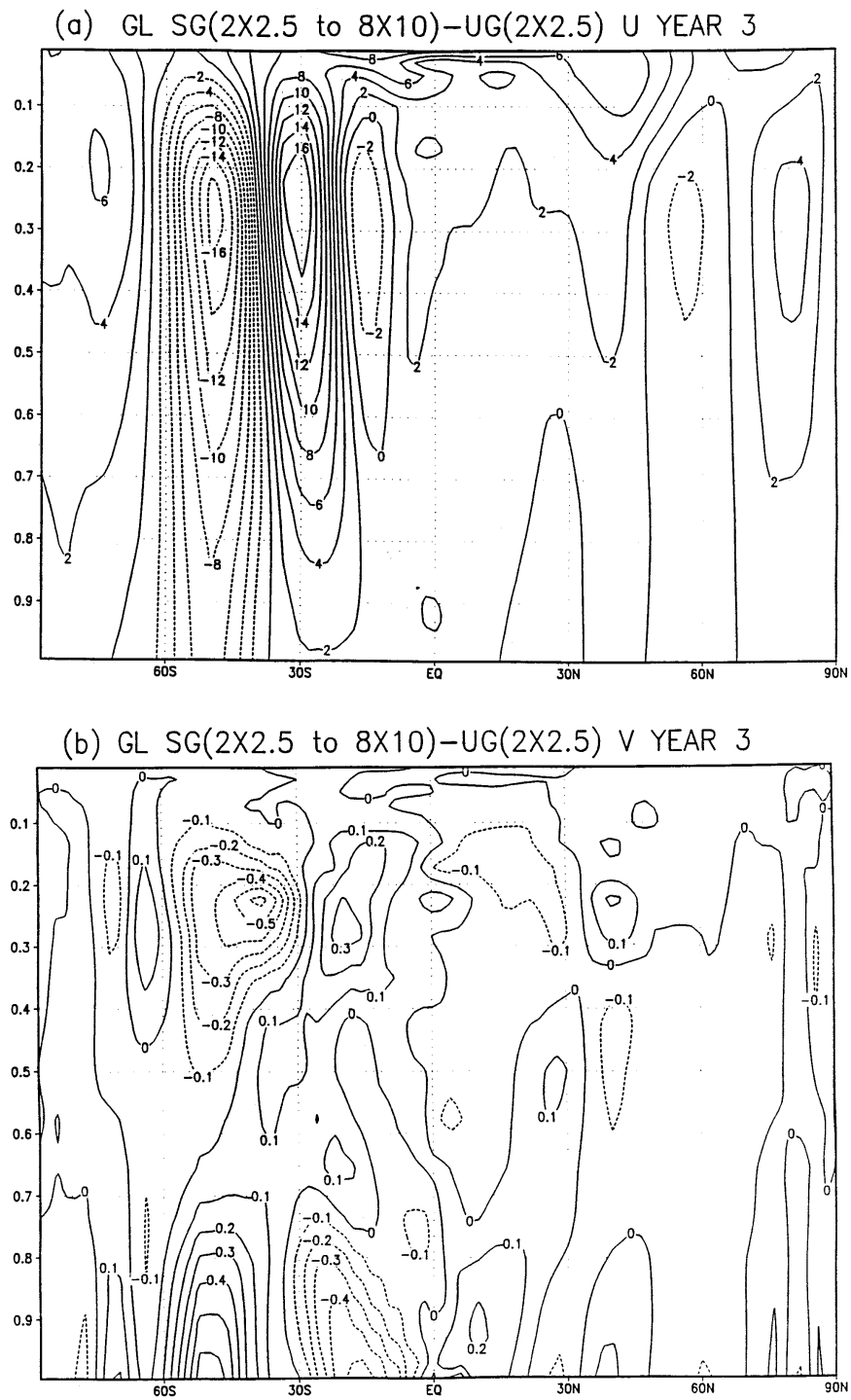


FIG. 7. The annual mean (year 3) differences between the stretched grid and control runs for the zonal U (a) and meridional V (b) wind components. The contour interval for (a) is 2 m s^{-1} and for (b) 0.1 m s^{-1} . The negative values are shown by dashed lines. The GL stands for the global domain.

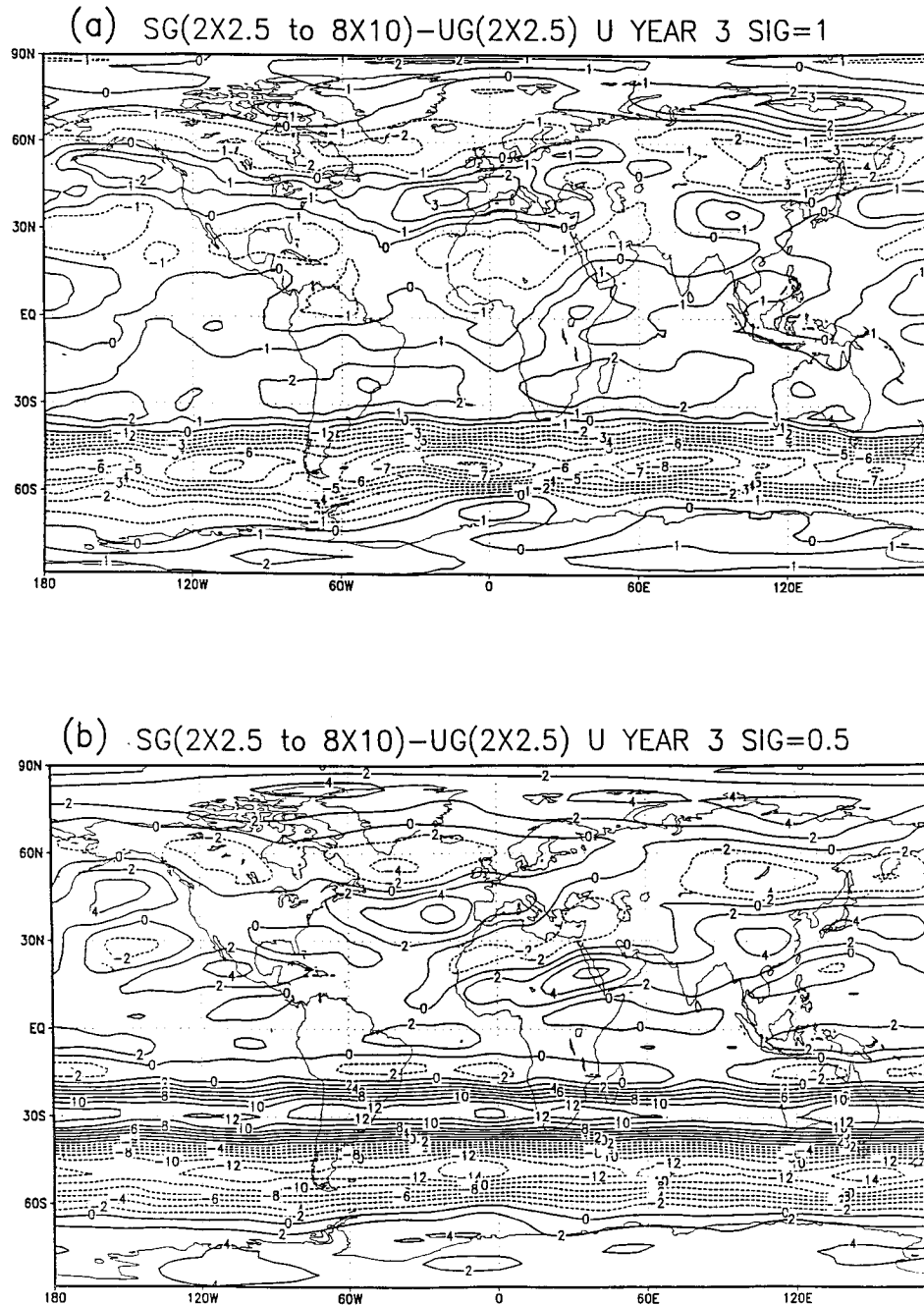


FIG. 8. The annual mean (year 3) differences between the stretched grid and control runs for the zonal wind component at the surface (a) and the $\sigma = 0.5$ or midtroposphere level (b). The contour interval is 1 m s^{-1} for (a) and 2 m s^{-1} for (b).

to 125°W . A bilinear interpolation is used to create initial conditions on a stretched grid.

For testing numerical procedures suitable for stretched grid model dynamics, we have chosen the July mean, or climate fields obtained from the 10-yr Atmospheric Model Intercomparison Project (AMIP) (Gates 1992) run with the GEOS GCM, with $4^\circ \times 5^\circ$ horizontal resolution, as initial conditions for depen-

dent variables. Initial conditions of this kind allow us to reduce the model spinup period as compared to a state of the rest (with zero initial winds) initial conditions used by Held and Suarez (1994). The climatological initial conditions used here produce strong disturbances in the beginning of the model integration, which are due to the differences between the GCM and the dynamical core such as the absence of

orography and simplified diabatic forcing. It allows us to investigate the robustness of the numerical technique used.

The results of any stretched grid model run are supposed to be compared with those of the corresponding control run performed with a global uniform fine-resolution grid. The purpose of the validation is to assess how well the stretched grid model is capable of describing the instantaneous regional and global scales and phenomena during medium-range integrations and representing mean circulation characteristics during long-term integrations. Also, for both medium-range and long-term integrations, it has to be verified that no noise and/or other unrealistic features are generated.

a. Filtering on a uniform fine-resolution global grid

As described above, in this case the stretched grid model is run with filtering on a fine-resolution global grid with the back and forth interpolation to the stretched grid at every time step. The $2^\circ \times 2.5^\circ$ resolution stretching to $8^\circ \times 10^\circ$ is used for the experiment. The eighth-order Shapiro filter is applied. The experiment is important for exposing the numerical problems related to grid irregularity. This seemingly simple filtering technique appeared to be incapable of providing the reliable noise control.

After several days of model integration, the prognostic fields are contaminated with strong small-scale computational noise (Fig. 4). The area of interest over the United States is not contaminated by noise. However, the noise pattern is most pronounced over the North Pole within the coarse-resolution grid boxes (Fig. 4a). Also, strong noise occurs over South Asia and the surrounding areas with strong initial gradients and, most importantly within the coarse latitudinal resolution grid boxes (Fig. 4b).

Actually, such a result should not be surprising. Small-scale features have been introduced as a result of the final interpolation back onto a stretched grid from the global uniform fine-resolution grid for which all filtering has been actually done. In other words, the filtering is done only for fine-resolution scales but not for those of the stretched grid. The small-scale noise features appearing within the stretched grid fields are not resolved for coarser-resolution gridboxes outside the fine-resolution area of interest. Namely, the filtering applied to the fine grid is not enough for the grid boxes with coarser resolution in one or both directions. Such noise is exacerbated over the areas with strong gradients resolved inadequately for the elongated grid boxes. The solution is not destroyed momentarily, as would be the case for the linear computational CFL instability. Instead, noise grows during several days of model integration before the solution is completely destroyed. The results of this ex-

periment, with globally uniform fine-resolution filtering, demonstrate the development of noise due to grid irregularity that cannot be reliably controlled by this version of the filtering procedure for a stretched grid model.

b. Uniform filtering directly on a stretched grid

The workable solution for the aforementioned computational problem related to grid irregularity is obtained by applying both the polar and Shapiro filters directly to the global stretched grid fields, without interpolating back and forth from the global uniform fine grid. As described above, the coordinate transformation following from (5) is introduced for grid points when using a stretched grid generator. All filtering is applied directly to the grid functions defined on the stretched grid, or for the grid transformed into a uniform one in the transformed coordinate system. The eighth-order Shapiro filter is used as in the previous experiment.

The results of the run with this filtering procedure are presented in Fig. 5. There is no indication of any computational noise generated during several days of the stretched grid model integration. Actually, this noise-free integration is continued in a climate mode, the results of which are discussed in the next section.

The obtained results show that computational noise generated by grid irregularity can be effectively controlled by basically the same filtering procedures as in the original dynamical core applied here to stretched grid prognostic fields.

c. Long-term benchmark integrations

The experiment discussed in section 4b and the corresponding control one with global uniform $2^\circ \times 2.5^\circ$ resolution have been run in a climate mode for 3 yr. The goal is to compare the benchmark experiment performed with a stretched grid and the control run with the uniform fine-resolution grid, in terms of temporal mean fields.

Vertical distributions of the zonal-mean zonal wind component are presented in Figs. 6a,b. Because of the symmetric hemispheric rhs forcing used in the dynamical core, both hemispheric jets are practically identical for the control experiment (Fig. 6b). The jet cores are positioned at approximately the $\sigma = 0.25$ level in the vertical and near the 40° – 45° latitude region in both hemispheres.

For the stretched grid run (Fig. 6a), with finer resolution in the Northern Hemisphere according to Fig. 3, the hemispheric jets are no longer symmetric. This is due to the fact that both computational errors and the actual rhs forcing in the dynamical core depend on resolution. For the Southern Hemisphere with coarser resolution, the jet gradients, pattern and configuration, especially in the Tropics, are somewhat

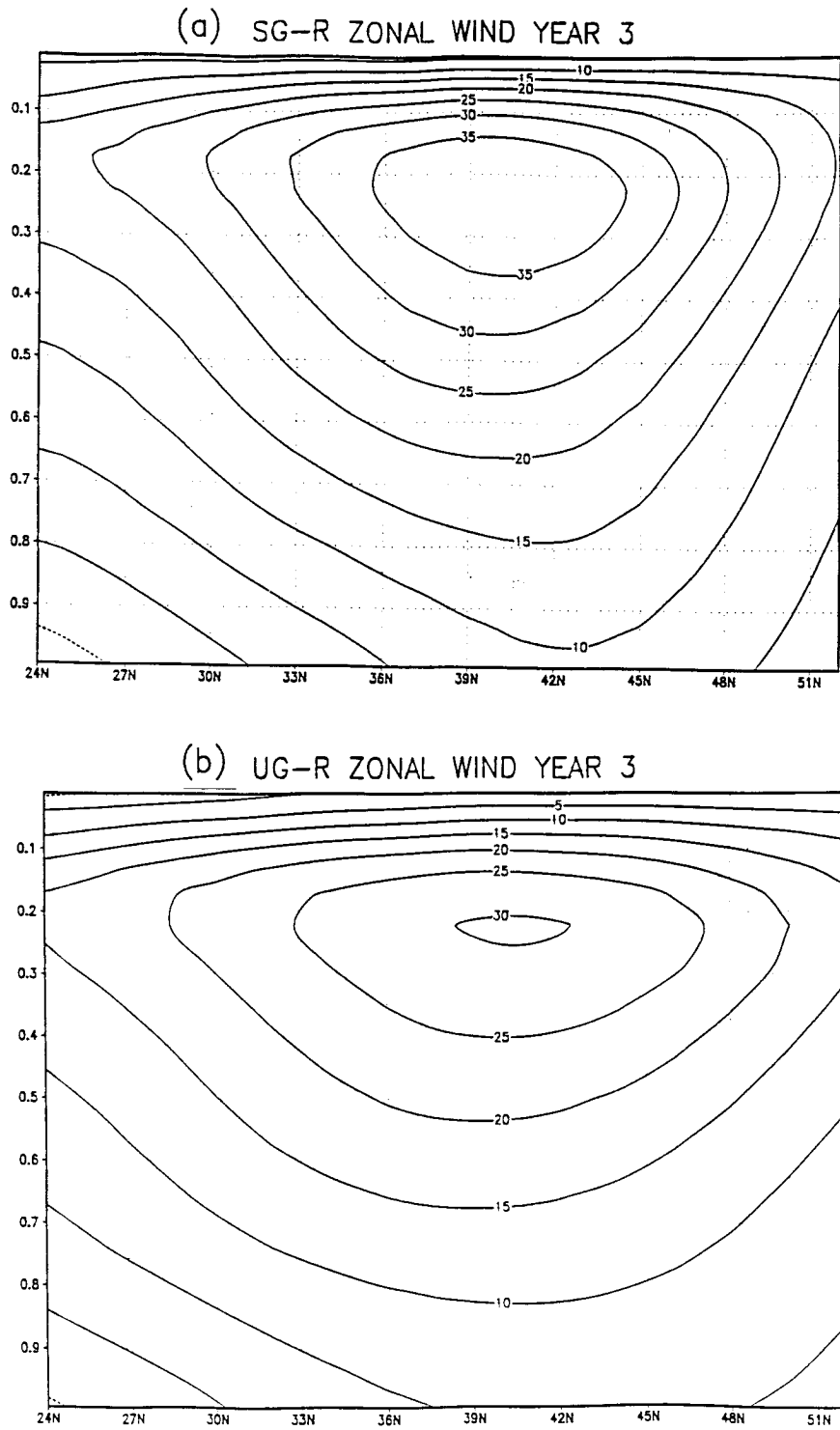


FIG. 9. The vertical σ -level distributions of the annual (year 3) mean wind component for (a) the zonal wind over the area of interest for the stretched grid run, (b) same as (a) but for the control uniform fine-resolution run, (c) the meridional wind over the area of interest for the stretched grid run, and (d) same as (c) but for the control uniform fine-resolution run. The contour interval for (a) and (b) is 5 m s^{-1} , and for (c) and (d) 0.2 m s^{-1} . The R (in SG-R and UG-R) stands for the region, or area of interest, located between 25° and 50°N , and 75° and 125°W .

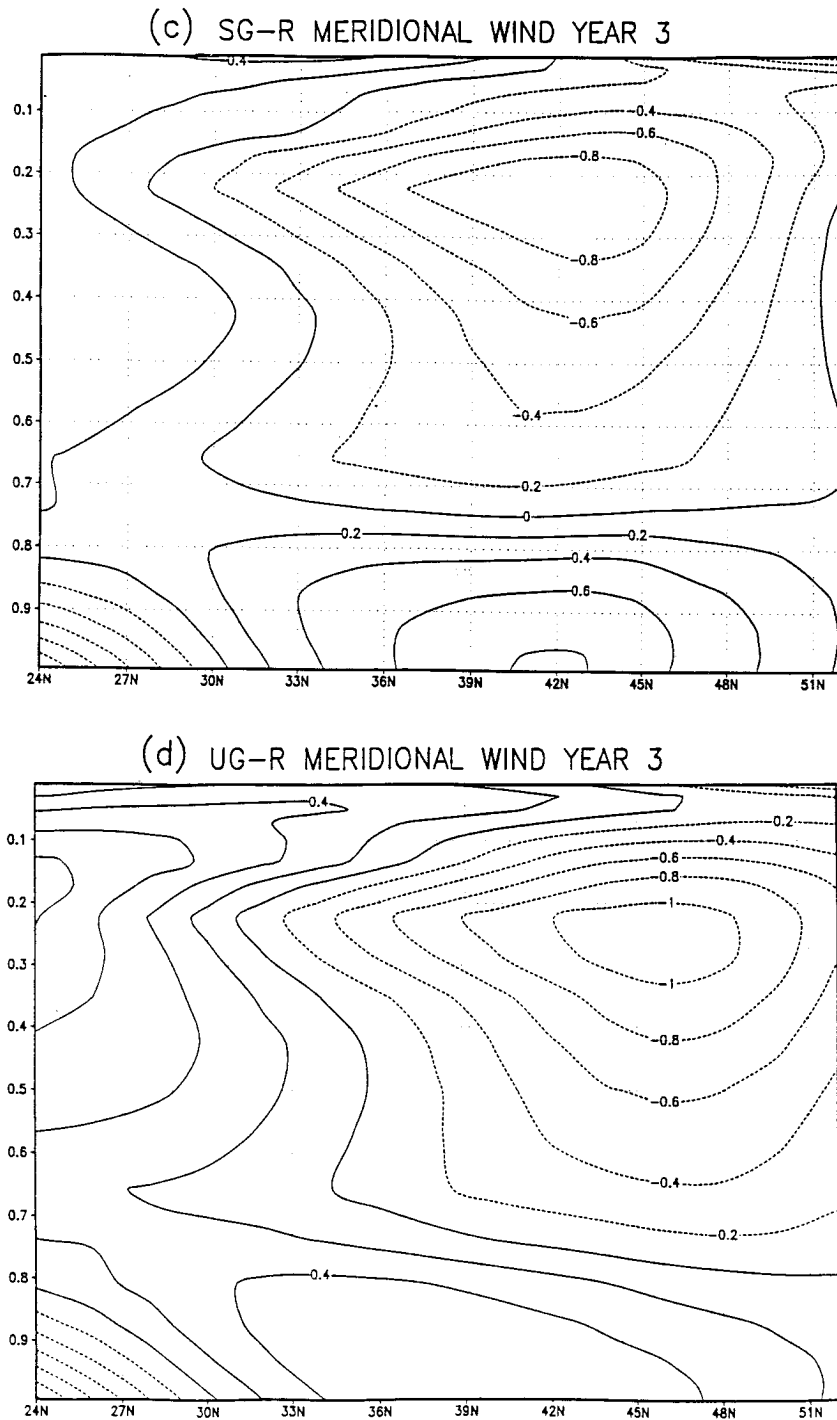


FIG. 9. (Continued)

different from those of the control run (Fig. 6b). Most importantly, the Southern Hemisphere jet core is overestimated by 5 m s^{-1} and is latitudinally shifted equatorward by approximately 10° . For the better resolved within the stretched grid Northern Hemisphere, the jet position and characteristics are very close to those of the control experiment (Figs. 6a,b). Similar results

are obtained for the vertical distributions of the zonal mean meridional wind component (Figs. 6c,d). In the better-resolved Northern Hemisphere, the meridional wind distribution for the Tropics and midlatitudes in the vicinity of the $\sigma = 0.25$ level for the stretched grid run (Fig. 6c) is close to that of the control run (Fig. 6d). It means that the Hadley cell is well rep-

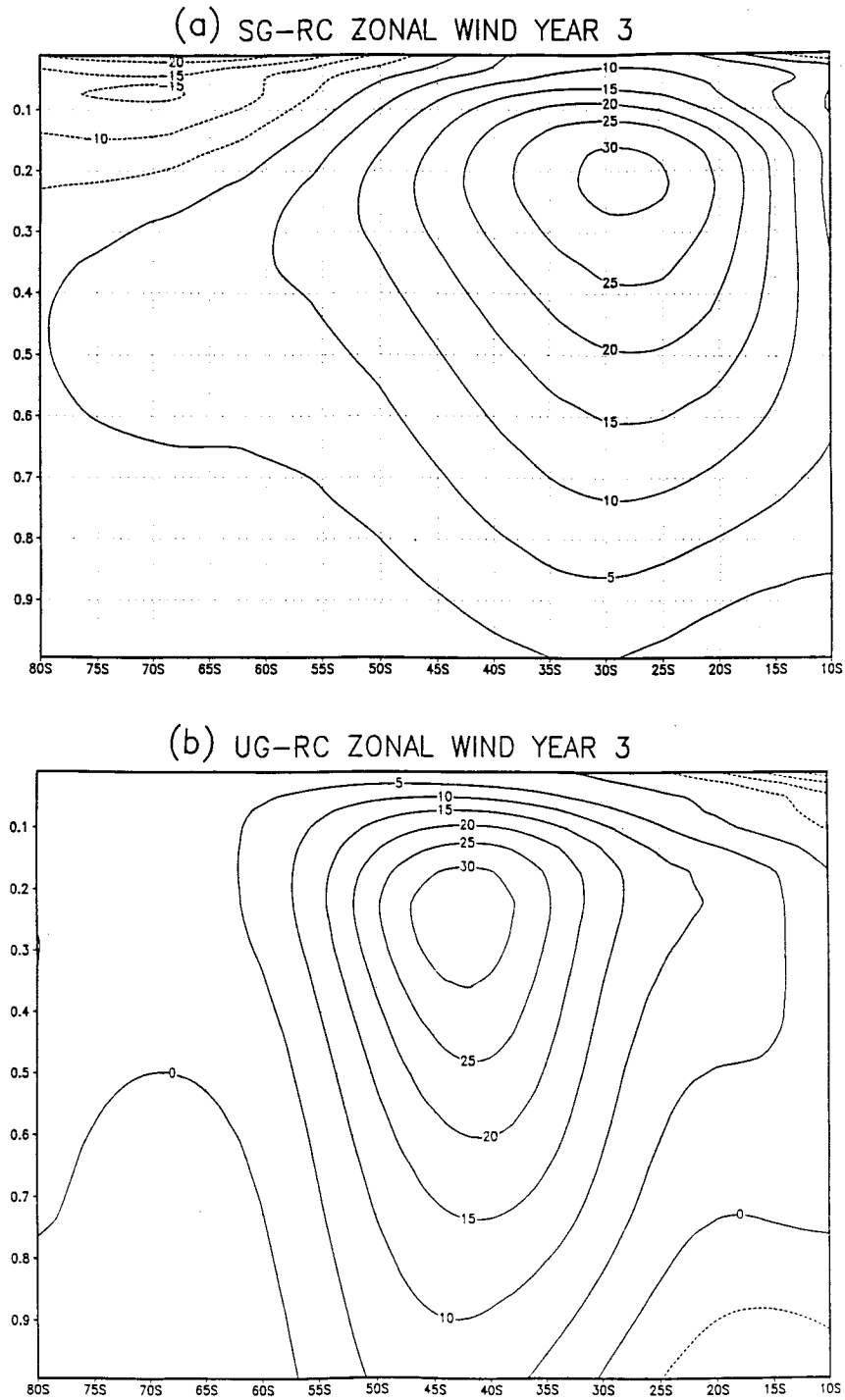


FIG. 10. Same as in Fig. 9 but for the area located within the least-resolved southeastern quadrant, between 10° and 80°S, and 0° and 150°E. The contour interval for (a) and (b) is 5 m s⁻¹, for (c) 0.3 m s⁻¹, and for (d) 0.5 m s⁻¹. The RC (in SG-RC and UG-RC) stands for the region with coarse resolution.

resented in the stretched grid run (Fig. 6c). For the Southern Hemisphere, the corresponding meridional wind distribution for the stretched grid run is underestimated (Fig. 6c). It results in weakening the Hadley

cell for the Southern Hemisphere with coarser resolution. Therefore, the results for each hemisphere strongly depend on hemispheric resolution.

The differences between vertical distributions of

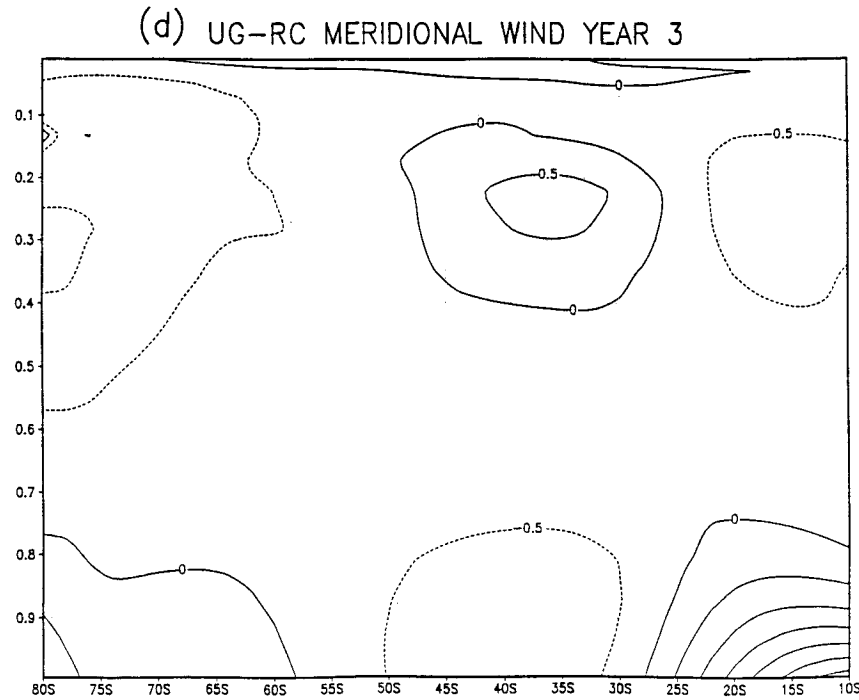
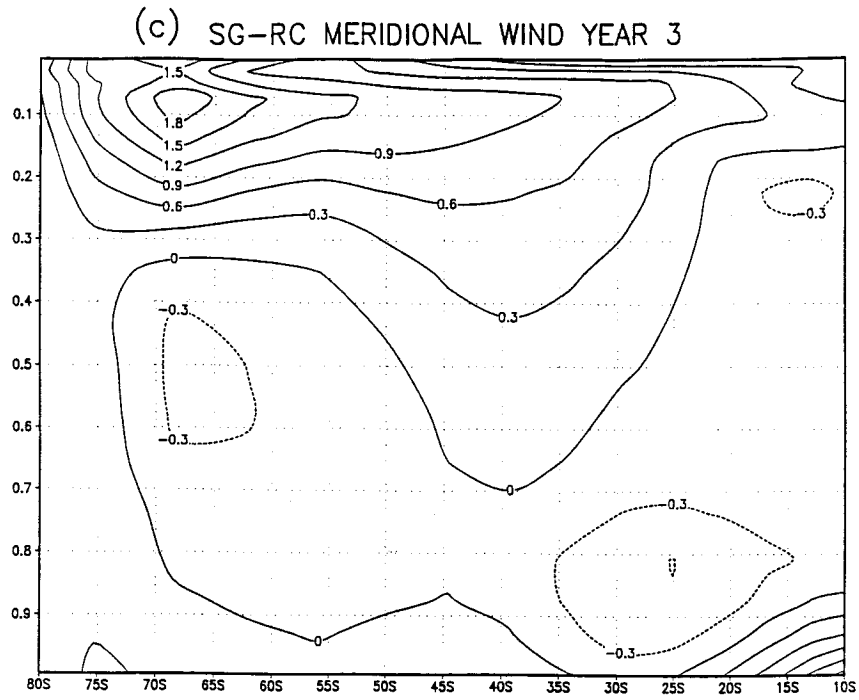


FIG. 10. (Continued)

the wind components shown in Fig. 6 are presented in Figs. 7a,b. These differences are calculated for the simulated stretched grid fields against the corresponding uniform fine resolution or control run fields. We are supposed to verify how close the results are of the stretched grid and control runs. The deviations

from the control run hereafter are called errors. We realize that these errors include a redistribution of the uncertainty due to, for instance, the differences between integrations started from slightly different initial conditions.

For the error calculation, the stretched grid fields

here and hereafter are interpolated onto the global uniform fine-resolution grid used for the control run. In the better resolved Northern Hemisphere, the errors are fairly small, mostly within $\pm 2 \text{ m s}^{-1}$ for the zonal wind U and $\pm 0.1 \text{ m s}^{-1}$ for the meridional wind V . For the Southern Hemisphere with coarser resolution, the errors are significant, almost an order of magnitude larger due to the equatorward shift of the jet and underestimation of the Hadley cell.

The annual mean errors for the stretched grid zonal winds for the $\sigma = 1$ and $\sigma = 0.5$ levels calculated as the differences between the stretched grid and control runs are presented in Figs. 8a,b. The errors are smaller over the best-resolved northwestern quadrant, for which they are mostly within $\pm 1\text{--}2 \text{ m s}^{-1}$ at the surface (Fig. 8a) and $\pm 2\text{--}4 \text{ m s}^{-1}$ for the middle troposphere (Fig. 8b). Within the northwestern quadrant, the errors are minimal for the area of interest over the United States, for which they are at least twice smaller than for the entire quadrant (Figs. 8a,b). Over other quadrants, especially over the Southern Hemisphere, the errors are significantly larger.

This conclusion can also be corroborated by considering the time-averaged zonal mean distributions of wind components over the fine-resolution area of interest (Fig. 9) located within the northwestern quadrant, and over the large area located in the least resolved southeastern quadrant (Fig. 10). For the area of interest, the patterns of the zonal and meridional wind vertical distribution are similar for both the stretched grid and control experiments. The vertical and latitudinal position and gradients of the jet core practically coincide (Figs. 9a,b), whereas the jet core strength is overestimated by 5 m s^{-1} in the stretched grid run. The corresponding patterns of the meridional wind vertical distribution are also close (Figs. 9c,d), although the negative feature is slightly underestimated by approximately 0.2 m s^{-1} , and its center is slightly shifted by approximately $1^\circ\text{--}2^\circ$ (i.e., by less than one grid interval) equatorward for the stretched grid run.

For the coarse-resolution area in the southeastern quadrant, the same circulation characteristics are profoundly different for the stretched grid and control experiments (Fig. 10). The jet core is shifted in the vertical upward by approximately 25–50 hPa and latitudinally by approximately $8^\circ\text{--}9^\circ$ equatorward for the stretched grid run (Figs. 10a,b). The jet patterns and gradients are also significantly different. The same is even more true for the meridional wind distributions (Figs. 10c,d). These results are consistent with those obtained for the GEOS GCM by Takacs and Suarez (1996) on the impact of coarser resolution or lower order of the accuracy of approximation.

The obtained results show the model sensitivity to variable horizontal resolution (over the Northern and Southern Hemispheres, for the global quadrants and over the area of interest) within a stretched grid. Most

importantly in the context of this study, they show the ability of a stretched grid model to reproduce climate patterns, especially over the area of interest and its vicinity, which are close to those of the control run with fine uniform global resolution. It appears that the regional circulation patterns and distributions are only moderately affected but not really overwhelmed by the incoming relatively poorly resolved flow.

5. Dynamical core integrations with enhanced variable resolution and large total global stretching factors

The results of stretched grid integrations presented above have been obtained with a total global stretching factor of 4 and rather coarse variable resolution for the grid stretching from $2^\circ \times 2.5^\circ$ to $8^\circ \times 10^\circ$. In view of the basic problems related to finite-difference approximations with nonuniform grids outlined in section 2, we should carefully verify the robustness of the numerical technique for stretched grids with larger total stretching factors. In this section, we present results of medium-range integrations of the stretched grid dynamical core with finer variable resolution and larger total global stretching factors ranging from 4 to 32. The same area of interest as in Fig. 3 is used for the experiments. The following variable horizontal resolution grids are used: $1^\circ \times 1.25^\circ$ stretching to $4^\circ \times 5^\circ$; $1^\circ \times 1.25^\circ$ stretching to $8^\circ \times 10^\circ$; $0.5^\circ \times 0.625^\circ$ stretching to $4^\circ \times 5^\circ$; $0.5^\circ \times 0.625^\circ$ stretching to $8^\circ \times 10^\circ$; $0.25^\circ \times 0.3125^\circ$ stretching to $4^\circ \times 5^\circ$; and $0.25^\circ \times 0.3125^\circ$ stretching to $8^\circ \times 10^\circ$. For validation purposes, two control experiment results, with fine uniform global $1^\circ \times 1.25^\circ$ and $0.5^\circ \times 0.625^\circ$ horizontal resolutions, are used. All these versions of fine-resolution stretched and uniform grids are run with the stronger fourth-order Shapiro filter and stronger polar filter [Eq. (10)]. Initial conditions are the same as in the benchmark integrations (the July mean fields from the AMIP run).

The results of the 10-day integrations with the total stretching factors of 4 and 8 for the global domain are presented in Fig. 11. Over the area of interest and the entire northwestern quadrant, both the control uniform grid and stretched grid runs are close to each other in terms of both the amplitude and phase of synoptic features even for the strong gradient area over the United States (Fig. 11a,b). The differences between the stretched grid runs and the control run over the area of interest are small, less than 1 K (Figs. 11c,d). The differences over the entire northwestern quadrant are also small, mostly within 2 K. At the same time, for other quadrants, especially over the least-resolved southeastern quadrant, the differences are much larger.

For a more detailed comparison, we consider the results of the 10-day integrations, with the total stretching factors of 4, 8, and 16, for the major part

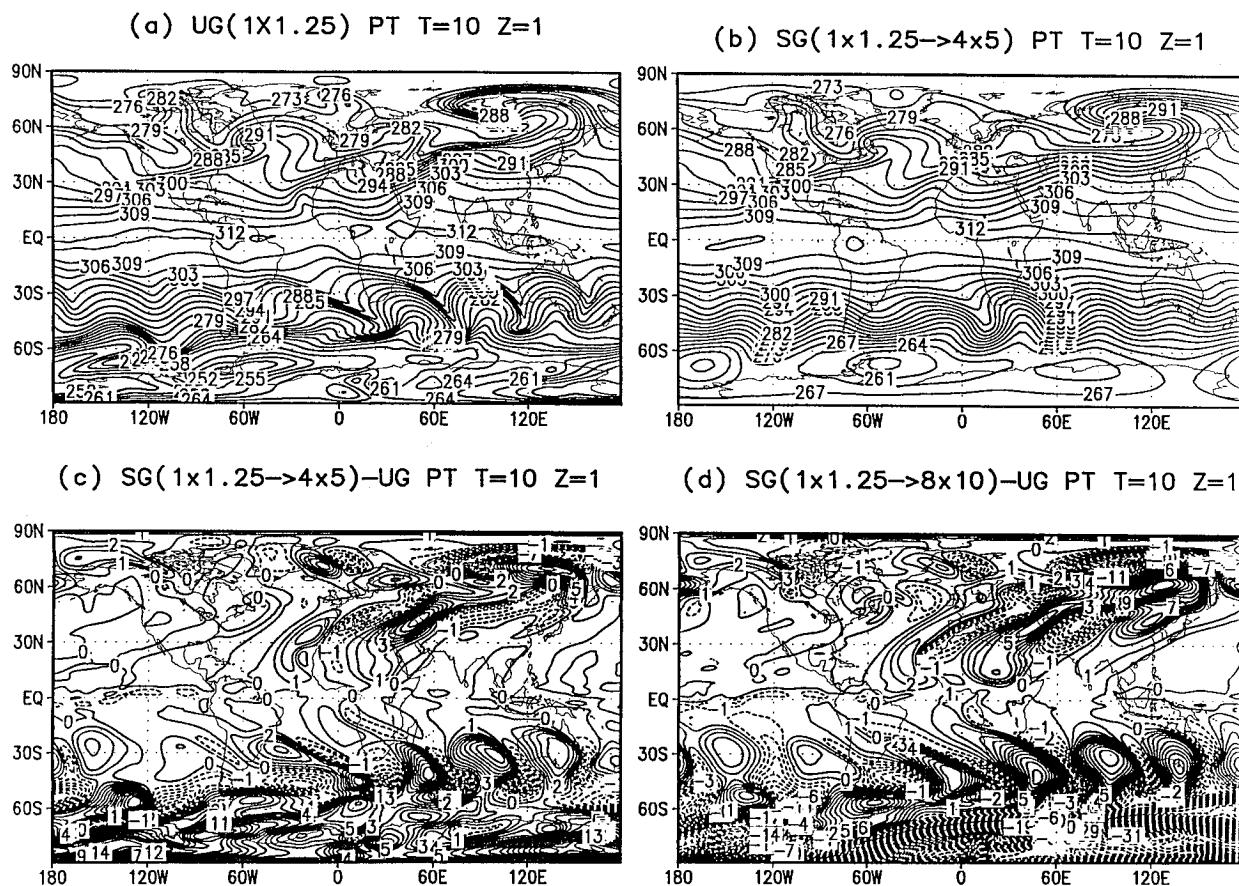


FIG. 11. The global surface potential temperature fields (a) and (b) and their differences (c) and (d) after 10-day integrations: (a) with the global uniform $1^\circ \times 1.25^\circ$ resolution grid (the control run); (b) with the grid stretching from $1^\circ \times 1.25^\circ$ resolution to $4^\circ \times 5^\circ$; (c) the difference field between (b) and (a); (d) the difference field between the run with the grid stretching from $1^\circ \times 1.25^\circ$ to $8^\circ \times 10^\circ$ and (a). The contour intervals for (a) and (b) are 3 K, and for (c) and (d) 1 K. The SG and UG stand for a stretched grid and uniform grid, correspondingly. The negative values are presented by dashed lines.

of the best-resolved northwestern quadrant that includes the area of interest and its large vicinity (Fig. 12). Two control experiment results, with uniform global resolution of $1^\circ \times 1.25^\circ$ (Fig. 12a) and $0.5^\circ \times 0.625^\circ$ (Fig. 12b), appeared to be well reproduced by the corresponding stretched grid runs [Figs. 12c,e (the left column) and Figs. 12d,f (the right column)] in terms of the position and depth for all centers, and in terms of the gradient strength. The fields obtained with the larger total stretching factors of 8 and 16 using the grids stretching from $1^\circ \times 1.25^\circ$ to $8^\circ \times 10^\circ$ (Fig. 12e) and $0.5^\circ \times 0.625^\circ$ to $8^\circ \times 10^\circ$ (Fig. 12f) are only slightly smoother than those of the corresponding control runs (Figs. 12a,b). The results of the integrations with the grids stretching from $1^\circ \times 1.25^\circ$ to $4^\circ \times 5^\circ$ (Fig. 12c) and $0.5^\circ \times 0.625^\circ$ to $4^\circ \times 5^\circ$ (Fig. 12d) represent even minor details of the corresponding control runs (Figs. 12a,b). The fields obtained with finer $0.5^\circ \times 0.625^\circ$ resolution over the area of interest (Figs. 12b,d,f) have smaller-scale features and stronger centers and gradients than those obtained with coarser $1^\circ \times 1.25^\circ$ resolution over the

area of interest (Figs. 12a,c,e). Notice that the computational costs are reduced by the factors of 6 and 10 for the total stretching factors of 8 and 16, relatively (as compared to the corresponding uniform grid control runs).

For the stretched grid runs, the deviations from the corresponding control runs or rms errors are calculated for all model sigma levels (Fig. 13). For both grids with total stretching factors of 4 and 8, the rms errors over the area or region of interest are small, although they are larger for the grid with the total stretching factor of 8. Over the entire best-resolved northwestern quadrant, the rms errors (Fig. 13c) are larger than those of the area of interest but are still quite moderate. Over the least-resolved southeastern quadrant, the rms errors are approximately an order of magnitude larger than those of the area of interest. For the stretched grid run with finer $0.5^\circ \times 0.625^\circ$ resolution over the area of interest stretching to $4^\circ \times 5^\circ$, or with the total stretching factor of 8, the rms errors (calculated against their corresponding control, or uniform $0.5^\circ \times 0.625^\circ$ resolution run) are similar

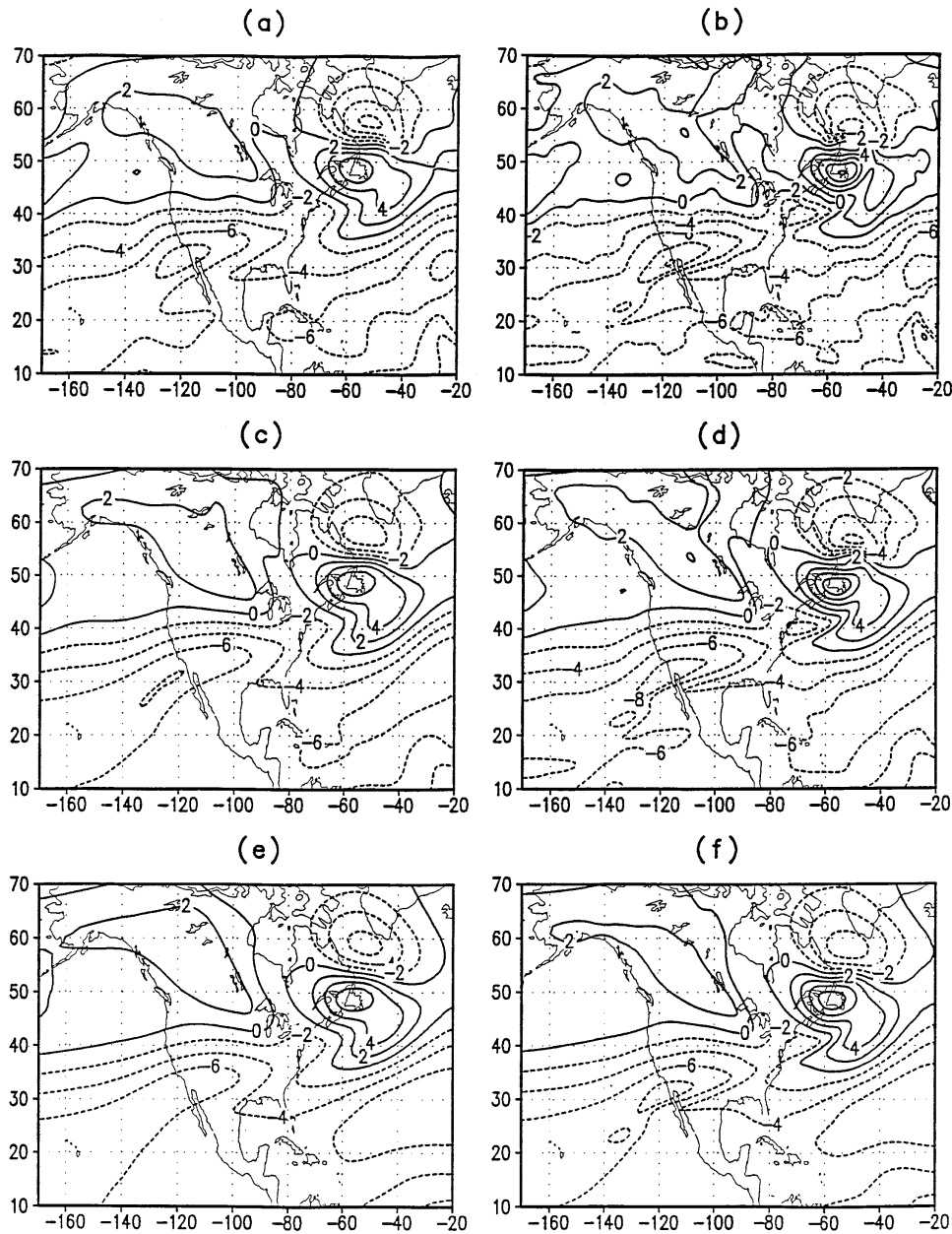


FIG. 12. The surface zonal wind fields after 10-day integrations for the large part of the northwestern quadrant (10° to 70°N and 20° to 170°W) using the grids with (a) global uniform $1^{\circ} \times 1.25^{\circ}$ resolution (the first control run), (b) global uniform $0.5^{\circ} \times 0.625^{\circ}$ resolution (the second control run), (c) $1^{\circ} \times 1.25^{\circ}$ resolution stretching to $4^{\circ} \times 5^{\circ}$ (the TSF of 4), (d) $0.5^{\circ} \times 0.625^{\circ}$ resolution stretching to $4^{\circ} \times 5^{\circ}$ (the TSF of 8), (e) $1^{\circ} \times 1.25^{\circ}$ resolution stretching to $8^{\circ} \times 10^{\circ}$ (the TSF of 8), and (f) $0.5^{\circ} \times 0.625^{\circ}$ stretching to $8^{\circ} \times 10^{\circ}$ (the TSF of 16). The TSF stands for the total stretching factor. The contour interval is 2 m s^{-1} .

but slightly smaller than those of the grid with the same total stretching factor of 8 but with the coarser $1 \times 1.25^{\circ}$ resolution over the area of interest.

Let us compare the spherical harmonic spectra for stretched grid integrations and the control one presented in Fig. 14. It is important to find out which spectral ranges are affected by introduction of global variable resolution. For both stretched grid integra-

tions, the large- and medium-scale spectral range (for the total wavenumbers less than or equal to 8) are very close to that of the control run. The result is important. These global spectral ranges should not be significantly affected by model variable resolution for medium-range integrations. The smaller scales show the impact of model variable resolution and filtering. The impact is stronger for the run with the larger total

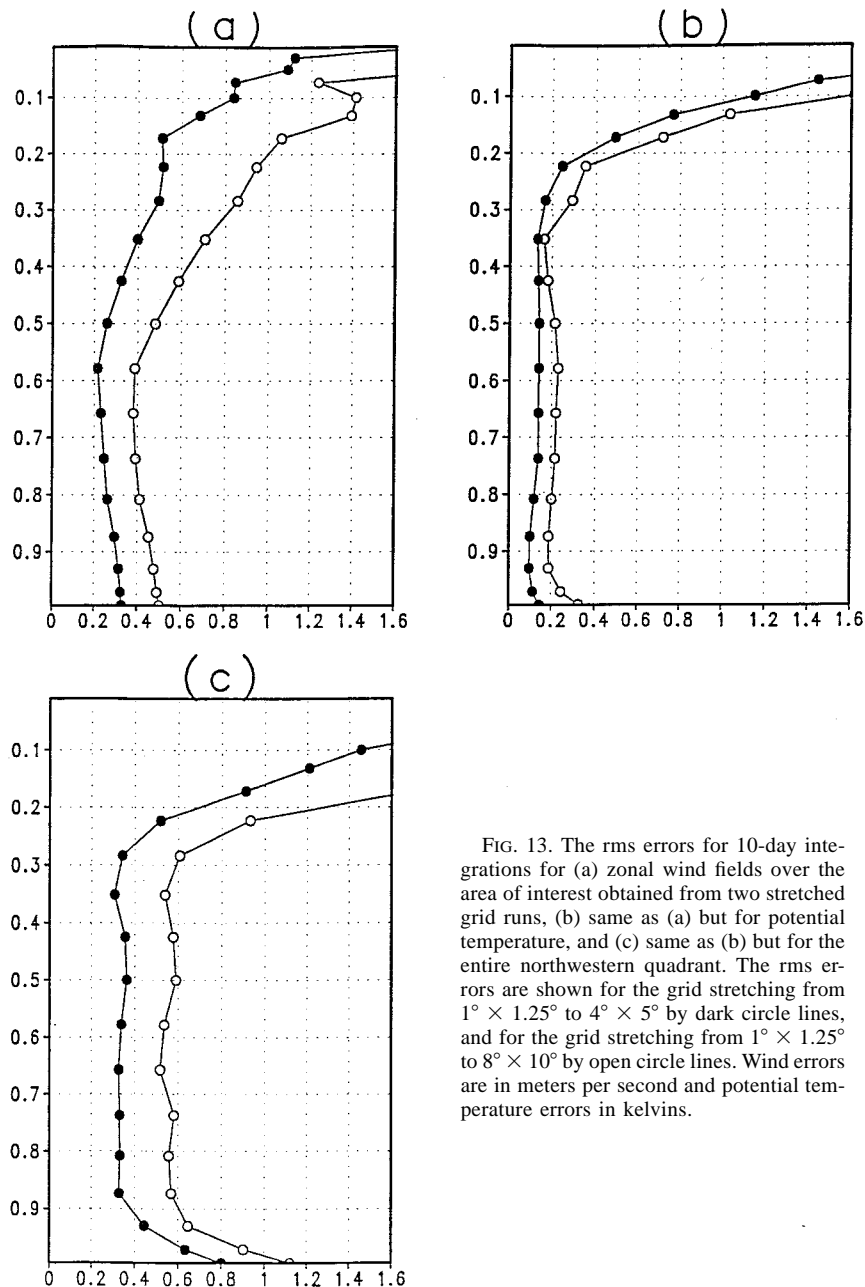


FIG. 13. The rms errors for 10-day integrations for (a) zonal wind fields over the area of interest obtained from two stretched grid runs, (b) same as (a) but for potential temperature, and (c) same as (b) but for the entire northwestern quadrant. The rms errors are shown for the grid stretching from $1^\circ \times 1.25^\circ$ to $4^\circ \times 5^\circ$ by dark circle lines, and for the grid stretching from $1^\circ \times 1.25^\circ$ to $8^\circ \times 10^\circ$ by open circle lines. Wind errors are in meters per second and potential temperature errors in kelvins.

stretching factor of 8. Notice that prior to spectra calculations the stretched grid fields are interpolated onto the corresponding global uniform fine-resolution grid that affects the smaller-scale spectral range.

Two more successful integrations have been performed using the grids with the very fine $0.25^\circ \times 0.3125^\circ$ resolution over the area of interest stretching to $4^\circ \times 5^\circ$ (with the total stretching factor of 16) and to $8^\circ \times 10^\circ$ (with the total stretching factor of 32). (The last grid has approximately the same number of grid points as the global uniform $1^\circ \times 1.25^\circ$ resolution grid.) The resulting fields are basically similar to those obtained with coarser reso-

lution over the area of interest. They contain smaller-scale features and stronger centers and gradients. However, it appeared to be too costly in terms of both the computer time and memory to perform the corresponding *control* run with the uniform global $0.25^\circ \times 0.3125^\circ$ resolution needed for calculating errors similar to those of Fig. 13.

Note that the requirements on consistent horizontal and vertical resolution pointed out by Lindzen and Fox-Rabinovitz (1989) should be applied within the stretched grid approach. Obviously, the resolution consistency within a stretched grid should be defined for the area of interest. The simplest way to implement

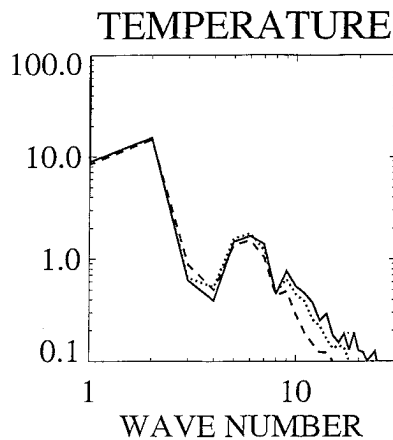


FIG. 14. The spherical harmonic spectra for the temperature fields at the $\sigma = 0.5$ level after 10-day integrations using the grids with the global uniform $1^\circ \times 1.25^\circ$ resolution (the control run) (solid line), the $1^\circ \times 1.25^\circ$ resolution stretching to $4^\circ \times 5^\circ$ with the total stretching factor of 4 (dotted line), and the $1^\circ \times 1.25^\circ$ resolution stretching to $8^\circ \times 10^\circ$ with the total stretching factor of 8 (dashed line).

it for the enhanced horizontal resolution region within a stretched grid is to consistently increase model vertical resolution globally. The associated additional computational cost is much less than that of increased horizontal resolution (with the corresponding decrease of a time step). Experiments on consistent resolution are planned to be performed later.

The close similarity between the stretched grid integrations and those of the corresponding control runs in a medium-range forecast mode, even for large total stretching factors presented in this section, shows the robustness and high quality of the numerical solutions obtained with variable resolution stretched grids.

The results presented in this and previous sections with various stretched grid model versions are encouraging. We can use the basic filtering procedure, readjusting only its parameters depending on resolution. Using the stretched grid approach allows us to take advantage of enhanced resolution and the corresponding downscaling over the area of interest for medium-range and long-range integrations.

6. Conclusions

The following conclusions are obtained as the result of the study.

- 1) The key result of the study with the variable-resolution dynamical core is that an adequate representation of regional scales, that is, a significant downscaling, is taking place over the area of interest (and its vicinity) not only for short-term integrations but also for medium-range and, most importantly, long-term integrations.
- 2) The stretched grid version of a finite-difference dynamical core with effective filtering techniques for nonuniform, stretched grids, is developed and

thoroughly tested. It allows one to reliably control computational noise arising from grid irregularity. The medium-range and long-term benchmark integrations of the stretched grid dynamical core have shown no negative computational effects accumulating in time. The positive impact from increased horizontal resolution, especially over the area of interest and its vicinity, is obtained. The regional prognostic fields and circulation patterns and distributions are not overwhelmed by the incoming relatively poorly resolved flow.

For long-term benchmark integrations, the particular emphasis is placed on ultimately using the stretched grid approach for regional climate modeling applications.

- 3) With adjusted basic filter parameters, stretched grids with medium to large total global stretching factors of 4 to 32 have been used. Successful medium-range integrations with summer climate initial conditions are performed for the grids with fine resolution over the area of interest (the United States) of $2 \times 2.5^\circ$, $1^\circ \times 1.25^\circ$, $0.5^\circ \times 0.625^\circ$, and $0.25^\circ \times 0.3125^\circ$ stretching outside the area of interest to $4^\circ \times 5^\circ$ or $8^\circ \times 10^\circ$. The profound similarity to the corresponding control runs with uniform fine global resolution is obtained.
- 4) Stretched grid integrations are performed at significantly reduced computational costs as compared to those of the corresponding global uniform fine-resolution ones. This allows one to use such fine resolution over the area of interest that is not possible otherwise for a foreseeable future.
- 5) The stretched grid dynamical core is planned to be introduced into the future stretched grid GEOS GCM.

Acknowledgments. The authors would like to thank Mr. R. Govindaraju for his programming support and Ms. M. Hall for typing the manuscript. The study has been supported by NASA Grant 578-41-11-20 and DOE Grant LWT6212307506. We would like to thank Dr. Kenneth Bergman, the NASA Program Manager, for his support of the study.

REFERENCES

- Anthes, R. A., 1970: Numerical experiments with a two-dimensional horizontal variable grid. *Mon. Wea. Rev.*, **98**, 810–822.
- , 1983: Regional models of the atmosphere in middle latitudes. *Mon. Wea. Rev.*, **111**, 1306–1335.
- Arakawa, A., and V. R. Lamb, 1981: A potential enstrophy and energy conserving scheme for the shallow water equations. *Mon. Wea. Rev.*, **109**, 18–36.
- , and M. J. Suarez, 1983: Vertical differencing of the primitive equations in sigma coordinates. *Mon. Wea. Rev.*, **111**, 34–45.
- Asselin, R., 1972: Frequency filter for time integrations. *Mon. Wea. Rev.*, **100**, 487–490.
- Berger, M., and J. Olinger, 1984: Adaptive mesh refinement for

- hyperbolic partial differential equations. *J. Comput. Phys.*, **53**, 484–512.
- Brown, J. A., and K. Campana, 1978: An economical time-differencing system for numerical weather prediction. *Mon. Wea. Rev.*, **106**, 1125–1136.
- Browning, M., O. Kreiss, and J. Olinger, 1973: Mesh refinements. *Math. Comput.*, **27**, 29–39.
- Burridge, D. M., and J. Haseler, 1977: A model for medium range weather forecasting-adiabatic formulation. European Centre for Medium-Range Weather Forecasts Tech. Rep., 63 pp. [Available from European Centre for Medium-Range Weather Forecasts, Shinfield Park, Reading RG2 9AX, United Kingdom.]
- Charney, J. G., 1966: Some remaining problems in numerical weather prediction. *Advances in Numerical Weather Prediction*, Travelers Research Center, 61–70. [Available from Archives and Special Collections Library, Building 14N-118, Massachusetts Institute of Technology, Cambridge, MA 02139.]
- , R. Fjortoft, and J. von Neuman, 1950: Numerical integration of the barotropic vorticity equation. *Tellus*, **2**, 237–254.
- Coté, J., M. Roch, A. Staniforth, and L. Fillion, 1993: A variable-resolution semi-Lagrangian finite-element global model of the shallow-water equations. *Mon. Wea. Rev.*, **121**, 231–243.
- Courtier, P., and J.-F. Geleyn, 1988: A global numerical weather prediction model with variable resolution: Application to the shallow-water equations. *Quart. J. Roy. Meteor. Soc.*, **114**, 1321–1346.
- Davies, H. C., 1976: A lateral boundary formulation for multi-level prediction models. *Quart. J. Roy. Meteor. Soc.*, **102**, 405–418.
- Déqué, M., and J. P. Piedelievre, 1995: High resolution climate simulation over Europe. *Climate Dyn.*, **11**, 321–339.
- Dietachmayer, G. S., and K. K. Droegemeier, 1992: Application of continuous dynamic grid adaption techniques to meteorological modeling. Part I: Basic formulation and accuracy. *Mon. Wea. Rev.*, **120**, 1675–1706.
- Fletcher, C. A. J., 1988: *Computational Techniques for Fluid Dynamics*. Vol. 2. Springer-Verlag, 541 pp.
- Fox-Rabinovitz, M. S., 1974: Economical explicit and semi-implicit integration schemes for forecast equations. *Sov. Meteor. Hydrol.*, **11**, 11–19.
- , 1988: Dispersion properties of some regular and irregular grids used in atmospheric models. Preprints, *Eighth Conf. on Numerical Weather Prediction*, Baltimore, MD, Amer. Meteor. Soc., 784–789.
- Gates, W. L., 1992: AMIP: The Atmospheric Model Intercomparison Project. *Bull. Amer. Meteor. Soc.*, **73**, 1962–1970.
- Giles, M. B., and W. T. Thompkins Jr., 1985: Propagation and stability of wavelike solutions of finite difference equations with variable coefficients. *J. Comput. Phys.*, **58**, 349–360.
- Gravel, S., and A. Staniforth, 1992: Variable resolution and robustness. *Mon. Wea. Rev.*, **120**, 2633–2640.
- Hardiker, V., 1997: A global numerical weather prediction model with variable resolution. *Mon. Wea. Rev.*, **125**, 59–73.
- Held, I. M., and M. J. Suarez, 1994: A benchmark calculation for the dry dynamical cores of atmospheric general circulation models. *Bull. Amer. Meteor. Soc.*, **75**, 1825–1830.
- Kalnay, E., M. Kanamitsu, J. Pfaendtner, J. Sela, M. Suarez, J. Stackpole, J. Tuccillo, L. Umscheid, and D. Williamson, 1989: Rules for the interchange of physical parameterizations. *Bull. Amer. Meteor. Soc.*, **70**, 620–622.
- Koch, S. E., and J. T. McQueen, 1987: A survey of nested grid techniques and their potential for use within the MASS weather prediction model. NASA Tech. Memo. TM-87808, 25 pp. [Available from National Technical Information Service, Springfield, VA 22161.]
- Kurihara, Y., 1965: Numerical integration of the primitive equations on a spherical grid. *Mon. Wea. Rev.*, **93**, 399–415.
- Lindzen, R. S., and M. S. Fox-Rabinovitz, 1989: Consistent vertical and horizontal resolution. *Mon. Wea. Rev.*, **117**, 2575–2583.
- Lorenz, E. N., 1960: Energy and numerical weather prediction. *Tellus*, **12**, 364–373.
- Mesinger, F., and A. Arakawa, 1976: Numerical methods used in atmospheric models. WMO/ICSU Joint Organizing Committee, GARP Publications Series 17, 64 pp. [Available from World Meteorological Organization, C. P. No. 2300, CH. 1211 Geneva 2, Switzerland.]
- Olinger, J., and A. Sundström, 1978: Theoretical and practical aspects of some initial boundary value problems in fluid dynamics. *SIAM J. Appl. Math.*, **35**, 419–446.
- Paegle, J., 1989: A variable resolution global model based upon Fourier and finite-element representation. *Mon. Wea. Rev.*, **117**, 583–606.
- Phillips, N. A., 1957: A coordinate system having some special advantages for numerical forecasting. *J. Meteor.*, **14**, 184–185.
- , 1959: An example of non-linear computational instability. *The Atmosphere and the Sea in Motion*, Rossby Memorial Volume, Rockefeller Institute Press, 501–504.
- , 1979: The nested grid model. NOAA Tech. Rep. NWS22, 80 pp. [Available from National Technical Information Service, Springfield, VA 22161.]
- Pielke, R. A., and Coauthors, 1992: A comprehensive meteorological modeling system—RAMS. *Meteor. Atmos. Phys.*, **49**, 69–91.
- Roache, P. J., 1976: *Computational Fluid Dynamics*. Hermosa Publishers, 446 pp.
- Robert, A., 1966: The integration of low order spectral form of the primitive meteorological equations. *J. Meteor. Soc. Japan*, **44**, 237–245.
- , and E. Yakimiw, 1986: Identification and elimination of an inflow boundary computational solution in limited area model integrations. *Atmos.–Ocean*, **24**, 369–385.
- Sadourny, R., 1975: The dynamics of finite difference models of the shallow water equations. *J. Atmos. Sci.*, **32**, 680–689.
- Schmidt, F., 1977: Variable fine mesh in a spectral global model. *Beitr. Phys. Atmos.*, **50**, 211–217.
- Schuman, F. G., 1971: Resuscitation of an integration procedure. NMC Office Note 54, 55 pp. [Available from National Center for Environmental Prediction/NOAA, 5200 Auth Road, Camp Spring, MD 20746.]
- Shapiro, R., 1970: Smoothing, filtering and boundary effects. *Rev. Geophys. Space Phys.*, **8**, 359–387.
- Skamarock, W. C., 1989: Truncation error estimates for refinement criteria in nested and adaptive models. *Mon. Wea. Rev.*, **117**, 872–886.
- , J. Olinger, and R. L. Street, 1989: Adaptive grid refinement for numerical weather prediction. *J. Comput. Phys.*, **80**, 27–60.
- Staniforth, A., 1995: Regional modeling: Theoretical discussion. WMO PWPR Report Series 7, WMO/TD-No. 699, 72 pp. [Available from World Meteorological Organization, C. P. No. 2300, CH. 1211 Geneva 2, Switzerland.]
- , and H. Mitchell, 1978: A variable resolution finite element technique for regional forecasting with primitive equations. *Mon. Wea. Rev.*, **106**, 439–447.
- , J. Coté, L. Fillion, and M. Roch, 1991: A variable-resolution finite-element semi-Lagrangian global model of the shallow water equations. Preprints, *Ninth Conf. on Numerical Weather Prediction*, Denver, CO, Amer. Meteor. Soc., 621–622.
- Suarez, M. J., and L. L. Takacs, 1995: Documentation of the Aries/GEOS Dynamical Core Version 2. NASA Tech. Memo. 104606, 103 pp. [Available from NASA, Goddard Space Flight Center, Greenbelt, MD 20771.]
- Takacs, L. L., and M. J. Suarez, 1996: Dynamical aspects of climate simulations using the GEOS GCM. NASA Tech.

- Memo. 104606, Vol. 10, 56 pp. [Available from NASA, Goddard Space Flight Center, Greenbelt, MD 20771.]
- , A. Molod, and T. Wang, 1994: Goddard Earth Observing System (GEOS) General Circulation Model (GCM) Version 1. NASA Tech. Memo. 104606 Vol. 1, 97 pp. [Available from NASA, Goddard Space Flight Center, Greenbelt, MD 20771.]
- Thompson, J. F., 1984: Grid generation techniques in computational fluid mechanics. *AIAA J.*, **22**, 1505–1523.
- , Z. U. A. Warsi, and C. W. Mastin, 1985: *Numerical Grid Generation: Foundations and Applications*. North-Holland, 483 pp.
- Vichnevetsky, R., 1987: Wave propagation and reflection in irregular grids for hyperbolic equations. *Appl. Numer. Math.*, **2** (1–2), 133–166.
- , and L. H. Turner, 1991: Spurious scattering from discontinuously stretching grids in computational fluid dynamics. *J. Appl. Math.*, **8**, 315–428.
- Wilhelmson, R. B., and C. S. Chen, 1982: A simulation of the development of successive cells along a cold outflow boundary. *J. Atmos. Sci.*, **39**, 1466–1483.
- Williamson, D., and G. L. Browning, 1974: Formation of the lateral boundary conditions for the NCAR limited area model. *J. Appl. Meteor.*, **13**, 8–15.
- Yakimiw, E., and A. Robert, 1990: Validation experiments for a nested grid-point regional forecast model. *Atmos.–Ocean*, **28**, 466–472.
- Yessad, K., and P. Benard, 1996: Introduction of a local mapping factor in the spectral part of the Meteo-France global variable mesh numerical forecast model. *Quart. J. Roy. Meteor. Soc.*, **122**, 1701–1719.